5 Kinematic boundary conditions and their influence on bivergent wedge evolution

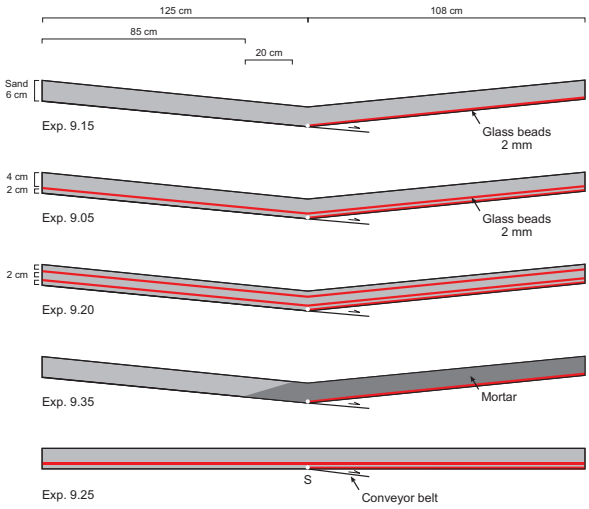

Figure 5.1: Kinematic boundary conditions of 1^{st} experimental series. Sand and glass-beads for all experiments were taken from one charge. Basal friction was the same in all experiments. Flexure was not simulated in experiment 9.25. Experiment number is used in text.

The following chapter intends to elucidate the influence of imposed kinematic boundary conditions such as a strength contrast across the singularity, different mechanic stratigraphies, and the degree of flexure on the kinematic evolution of bivergent sand-wedges. Special emphasis shall be laid upon the strain transfer between the pro- and the retro-wedge as well as the timing and magnitude of strain accumulation within the pro-wedge. An account on the kinematic evolution of the reference experiment is provided first, followed by a description of four other experiments which differ with respect to their kinematic boundary conditions (Fig. 5.1).

5.1 Reference experiment

Kinematic evolution of a bivergent sand-wedge. Based on visual inspection of the reference experiment, the kinematic evolution of a bivergent sand-wedge is divided into four stages. In stage I, initial layer parallel shortening leads to the formation of two conjugate shear zones, which nucleate at the singularity and define thus a symmetric pop-up (Fig. 5.2a). Further convergence leads to rapid surface uplift associated with progressive back tilting of this pop-up towards the upper plate. During stage II, three narrowly spaced thrust faults form successively within the pro-layer (Fig. 5.2b, c). They nucleate as well at the velocity discontinuity and are carried passively back- and upwards in the hangingwall of the retro shear-zone throughout the remaining experiment. Stage II marks thus the transition from a symmetric to an asymmetric topographic and kinematic state. At this stage surface uplift rates of the axial-zone and the retro-wedge are still high but start to decrease (Fig. 5.3), while rates of thrusting along the retro shear-zone remain constant. With continued convergence, the topographic load of the axial-zone and the retro-wedge increases until a critical height is reached. At this point, i. e., after $\sim 30\,cm$ of convergence (Fig. 5.2d, e), the axial-zone and the retro-wedge provide a sufficient load to initiate a basal detachment, which ramps up through the pro-layer to finally form a flat-topped box anticline – stage III commences. Lateral growth of the pro-wedge is now attained by a forward-breaking sequence of flat-topped box anticlines, which is hereafter referred to as frontal accretion. The respective basal detachment is located within the lowermost part of the pro-layer and thus a few millimeters above the conveyor belt. During stage III, rates of thrusting along the retro shear-zone remain fairly constant (Fig. 5.3). However, rates of the lateral growth of the pro-wedge, as well as surface uplift rates of both the axial-zone and the retro-wedge do fur-

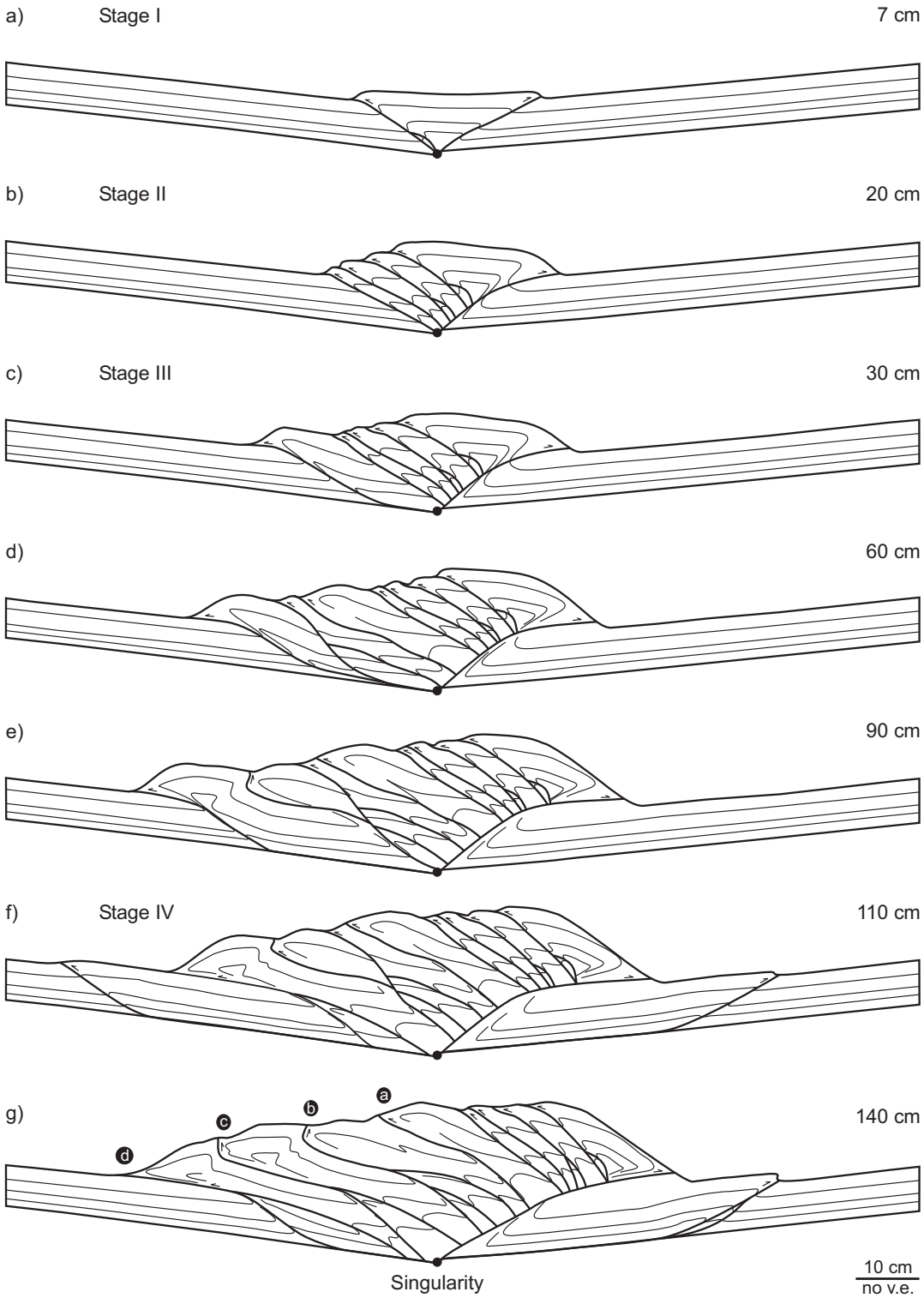

Figure 5.2: Line drawings of sequential stages of the reference experiment (9.15). Numbers on the right are *cm* of convergence. Frontal accretion within the retro-wedge occurs after $\sim 100\,cm$ of convergence (stage IV). Label ⓐ to ⓓ denote thrusts.

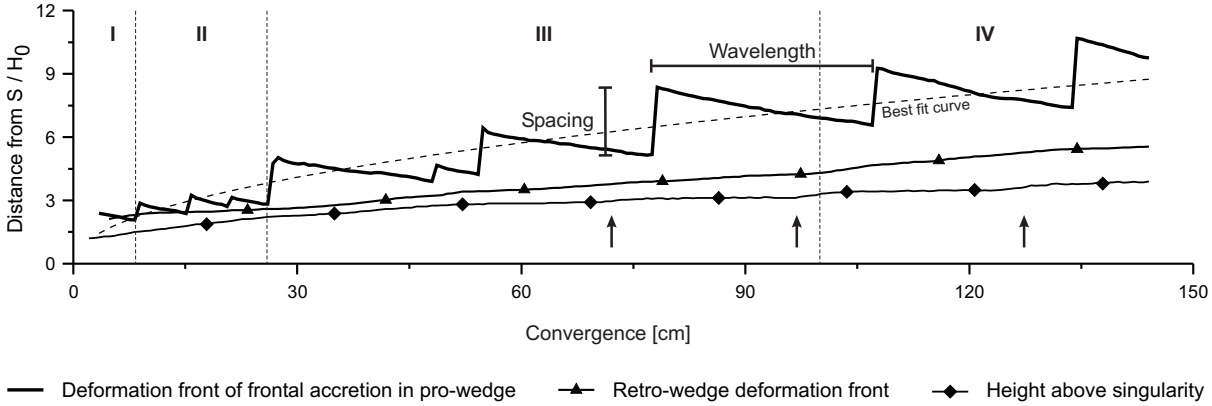

Figure 5.3: Evolution of geometric parameters as defined in figure (4.11), taken from the PIV images at every 1.5 *cm* of convergence. Arrows point to times of accelerated vertical growth, which predate the formation of a new thrust within the pro-layer. Dashed line is the best fit curve for the propagation of deformation of frontal accretion within the pro-wedge: $y = 0.79t^{0.48}$ with $R^2 = 0.88$; y is the normalised distance between the deformation front of frontal accretion within the pro-wedge and the singularity and t is convergence [*cm*]. Roman letters and vertical dotted lines indicate duration of the four stages of bivergent wedge evolution. Graphic definition of spacing as the horizontal distance between the previous and the newly formed deformation front; and wavelength as the time in *cm* convergence between two successive thrust initiations.

ther decrease. Additionally, the latter is disturbed by discrete, short-lived accelerations, which predate the formation of a new thrust within the pro-layer. After $\sim 100\,cm$ of convergence, frontal accretion within the retro-wedge commences and marks thus the onset of stage IV. Continued convergence is now taken up by two frontal accretion systems (Fig. 5.2f, g), indicating that the wedge starts to regain its initial symmetric conditions. This results in a further slowdown of the lateral growth rate of the pro-wedge (Fig. 5.3). It follows from the above description that the propagation of deformation within the pro-wedge, i. e., its lateral growth, is attained by the cyclic formation of flat-topped box anticlines at its toe. The resulting overall trend is best described by a power law (Fig. 5.3). Accordingly, the pro-wedge grows proportional to the convergence (t) by $t^{0.48}$ ($R^2 = 0.88$), which is close to the theoretically predicted value of $t^{0.5}$ (Dahlen, 1990).

Topographic evolution. Given an Eulerian reference frame, two domains of the spatio-temporal distribution of incremental surface uplift are distinguished within the bivergent sand-wedge. One comprises the pro-wedge and one includes the axial-zone and the retro-wedge. ISU in the former is highly variable and shows discrete accelerations, while the latter is characterised by an almost concentric growth (Fig. 5.4, Fig. 5.5). As noted in section (4.4), several ways to read ISU maps exist:

Time- and location-lines indicate the high spatial or temporal variability of ISU for a given time interval or position in a Eulerian reference frame. The initiation of individual flat-topped box anticlines is associated with a maximum ISU right above the respective ramp segment. Thus, propagation of these ISU maxima through time and space reflects the propagation of deformation within the pro-wedge. While convergence proceeds, new thrust faults are formed and older ones are abandoned. This is coeval with a decay of ISU for a given ramp segment. However, almost all ramp segments identified in figure (5.5) show a renewed increase in ISU, which suggests their re-activation. The respective increase can gain an order of magnitude without any modifications of the imposed kinematic boundary conditions (Fig. 5.5). Therefore, lines which follow individual ramp segments are referred to as thrust

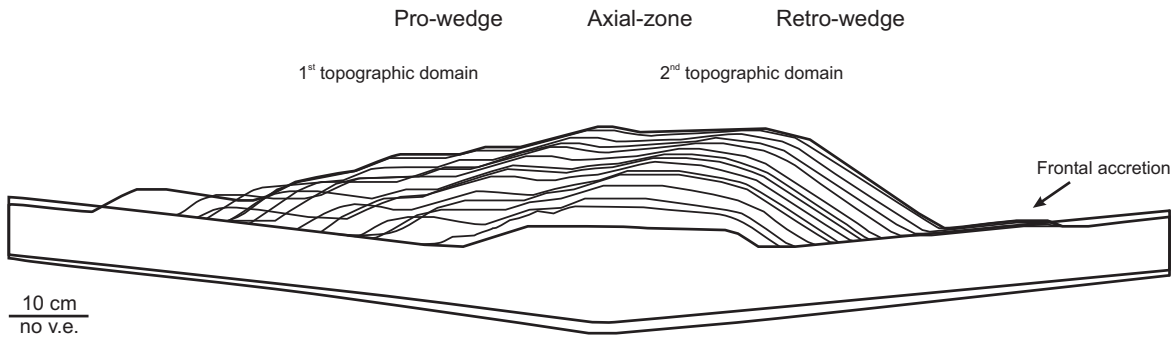

Figure 5.4: Topographic evolution of reference experiment. Outlines were taken at every 10 *cm* of convergence. The first, i. e., after 10 *cm* and the last, i. e., after 150 *cm* of convergence outline are given in complete form, to indicate the magnitude of flexure. Two topographic domains mirroring two different growth modes can be distinguished. Cyclic accretion within the pro-wedge results in distinct steps in topography, whereas continuous addition of pro-wedge derived material to the axial-zone and the retro-wedge leads to a nearly concentric growth.

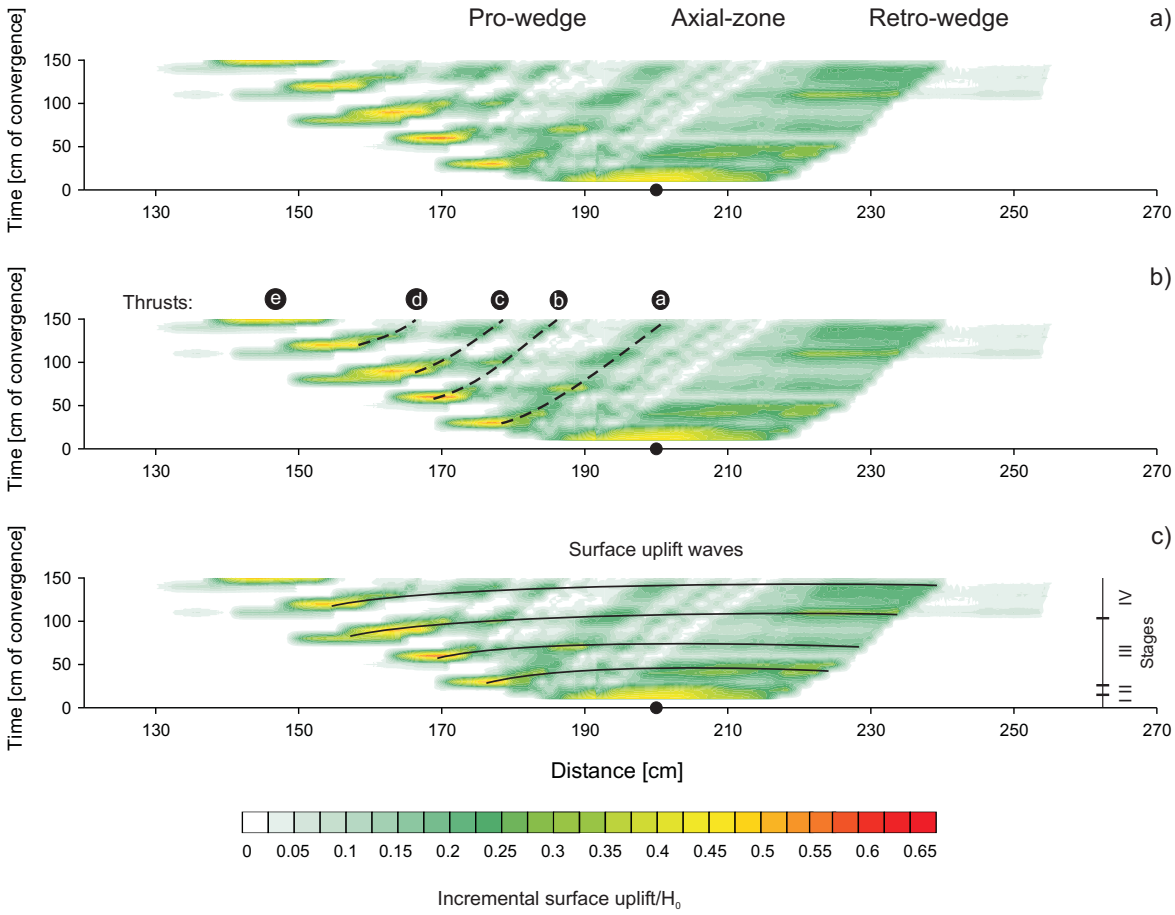

Figure 5.5: Incremental surface uplift of reference experiment. (a) Raw data, see figure (4.13) for derivation. (b) Dashed lines follow surface uplift traces of ramp segments of forethrusts. Re-activation of thrusts can result in an increase of ISU by one order of magnitude. For location of thrusts ⓐ to ⓓ see figure (5.2g). (c) Bold lines follow surface uplift waves, which are tightly linked with the accretion cycle.

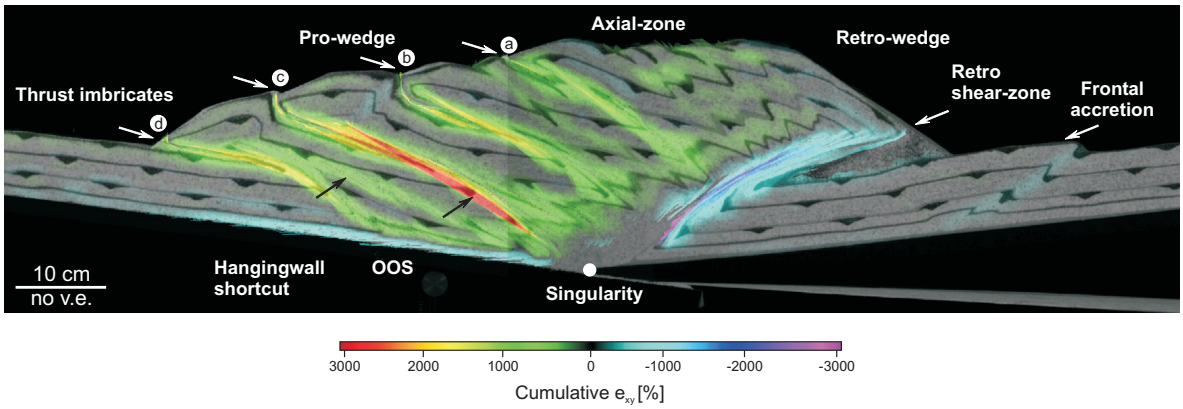

Figure 5.6: Distribution of finite e_{xy} for the reference experiment after 140 cm of convergence.

traces. It is furthermore pointed out, that at times of maximum ISU within the pro-wedge the respective magnitudes of ISU within the axial-zone and the retro-wedge are at their minimum. This observation led to the discovery of very subtle surface uplift waves, which are intimately linked to the accretion cycle. Thereby, the initiation of each thrust within the pro-layer is associated with maximum ISU. With ongoing convergence, this maximum migrates as a wave, with decreasing magnitude through the entire wedge until it has reached the tip of the retro-wedge deformation front. At this stage a new thrust in the pro-layer is formed, which again is followed by a similar surface uplift wave. This observation agrees well with the finding that the height above the singularity shows discrete accelerations just before a new thrust within the pro-layer is formed (Fig. 5.3).

Finally, ISU mirrors the four stages of bivergent-wedge evolution, as outlined above. In stage I ISU is symmetrically distributed above the singularity, while during stage II the location of maximum ISU shifts towards the lower plate and results thus in a topographic asymmetry. The former is further magnified during stage III, especially, if the ISU maxima associated with the initiation of the thrusts, are considered. Frontal accretion within the retro-wedge (stage IV) marks the transition to a more symmetric wedge-topography.

Strain accumulation. Based on the displacement field derived from PIV analysis, finite strain after 140 cm of convergence was calculated, to obtain a wedge-scaled view on strain accumulation (Fig. 5.6). The distribution of finite strain clearly images the main structural elements such as the basal detachment, the retro shear-zone and individual thrust imbricates. Within the pro-wedge a systematic distribution of finite strain was recognised: thrusts located at either the toe or the rear of the pro-wedge show only minor magnitudes of finite strain. In turn, thrusts positioned close to the prominent topographic break within the pro-wedge show significantly higher finite strain magnitudes. It is also pointed out that the magnitude of retro shear is highest at the retro shear-zone which separates lower plate from upper plate material and is thus interpreted as long-lived.

A more detailed insight to strain accumulation at the thrust-scale is derived from the EDM. Based on the EDM, the main structural elements such as the initial pop-up, the retro shear-zone, individual thrust imbricates within the pro- and the retro-wedge as well as subtle features like backthrusts, footwall shortcuts and out-of-sequence reactivation of thrusts can be identified (Fig. 5.7).

The proposed four stages in bivergent-wedge evolution can be deduced from figure (5.7) as well. The transition from stage I to stage II can be iden-

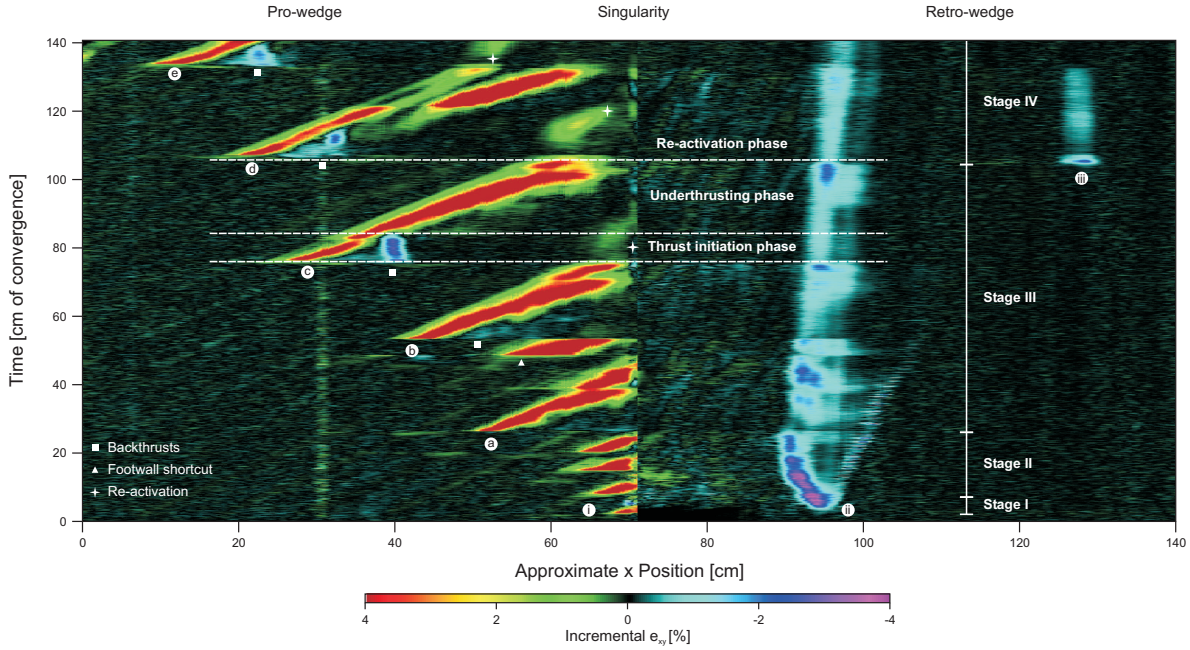

Figure 5.7: Evolution of deformation for the reference experiment. Labels ⓐ to ⓔ refer to forethrusts within the pro-wedge. See figure (5.2g) for location and figure (4.14) for derivation. ⓘ denotes the pro-shear of the initial pop-up, ⓘⓘ the respective retro-shear and ⓘⓘⓘ denotes the frontal accretion within the retro-wedge. Four stages of bivergent wedge evolution as well as phases of accretion cycle are explained graphically. Note, pulsating but decreasing activity of retro-shear zone.

tified, since the life-span of the three narrowly spaced thrusts is significantly longer, than the life-span of the fore-thrust bounding the initial pop-up. The transition from stage II to stage III is more pronounced, since the flat-topped box anticlines have a significantly longer life-span than the three fore-thrusts. Incremental e_{xy} along the retro shear-zone decreases markedly as well, but shows pulses, which predate the formation of a new thrust within the pro-layer. These strain pulses agree well with the ISU waves described above. The onset of stage IV is marked by the emergence of frontal accretion within the retro-wedge. Coevally, re-activated thrusts accumulate more, the retro shear-zone less incremental e_{xy}, whereby the latter still shows incremental e_{xy} pulses.

The accretion cycle. Further analysis of the EDM revealed a regular, incremental e_{xy} pattern, which is referred to as the accretion cycle. Although e_{xy} was calculated from the velocity field, e_{xy} is considered to be better suited for the description of an accretion cycle than the horizontal (v_x) or the vertical (v_y) component of the velocity field. However, key observations concerning either v_x or v_y are indicated were appropriate. Each accretion cycle is thought to consist of three phases: a thrust initiation phase, which in turn is divided into three sub-phases; an underthrusting phase; and a re-activation phase, where the latter is coeval with the thrust initiation phase of the following accretion cycle. The nomenclature of the first two phases follows Gutscher et al. (1998) and Hoffmann-Rothe et al. (2004), whereas the term re-activation phase is introduced here.

During the first sub-phase of the thrust initiation phase, deformation propagates outward along the basal detachment and finally steps up to form a symmetric pop-up. The respective backthrust terminates right at the tip of the previous deforma-

tion front (Fig. 5.8b). Although, not very well localised, this pop-up evokes a significant decrease of v_x within the pro-layer (Fig. 5.8h). Interestingly, this pop-up has no topographic expression, but it clearly stands out in the diagram showing the vertical component of the velocity field (Fig. 5.8n).

During the second sub-phase of the thrust initiation phase, the basal detachment and the forethrust of the pop-up form a continuous shear-zone with a flat-ramp geometry. Coevally, the backthrust associated with the pop-up and the previous deformation front cease in activity (Fig. 5.8c).

In the third sub-phase of the thrust initiation phase, the initial pop-up evolves into a flat-topped box anticline, which is associated with the formation of a backthrust. Convergence is now taken up by the newly formed forethrust, its backthrust, the previous forethrust, and the retro shear-zone (Fig. 5.8d). With respect to the first sub-phase, no significant change of the components of the velocity field occurred during the latter two sub-phases.

In the following underthrusting phase, the backthrust and the previous deformation front are abandoned and the pro-layer is considerably overthrusted by the pro-wedge. Convergence is now taken up by two conjugate shear-zones, which define a wedge-scaled, symmetric pop-up (Fig. 5.8e). Thereby, the frontally accreted material is continuously transferred towards the axial-zone, rotated back and finally passively uplifted in the hangingwall of the retro shear-zone. Consequently, v_x is at its maximum within the axial-zone and decreases towards the pro- and the retro-wedge (Fig. 5.8m, q). It follows that the location of maximum v_y has moved from the flat-topped box anticline at the toe of the pro-wedge towards the axial-zone. This observation agrees well with the ISU wave documented earlier. However, the location of maximum v_y during subsequent underthrusting phases is systematically shifted from the axial-zone during early accretion cycles towards the center of the pro-wedge during later accretion cycles (Fig. 5.8m, q).

The underthrusting phase is terminated by the thrust initiation phase of the next accretion cycle. Note again, that prior to the formation of a new thrust imbricate within the pro-layer, strain accumulation increases significantly along the retro shear-zone (5.7). During the second sub-phase of the thrust initiation phase, incremental e_{xy} ceases to accumulate along the previous deformation front, but is re-activated during the respective third sub-phase (Fig. 5.8f). The previous deformation front remains active until the next underthrusting phase commences. Note, that during the underthrusting phase, the difference between both velocity components, i. e., $v_x - v_y$ remains nearly constant, but is highly variable during the thrust initiation and the re-activation phase (Fig. 5.9, Fig. 5.8a).

The evolution of incremental e_{xy} at points located within individual ramp segments of either the fore-thrusts or the retro shear-zone shows one absolute and two local maxima which can be linked with the three phases of the accretion cycle identified above (Fig. 5.10). Within this respect, the two local maxima correspond to the thrust initiation phase and the re-activation phase respectively, whereby the former attains higher magnitudes than the latter. The absolute maximum is linked with the underthrusting phase. These observations suggest that each phase within an accretion cycle is associated with different magnitudes and rates of strain accumulation. In addition, the strain history of the retro shear-zone follows a pattern, which can be best described by a damped oscillation. Thereby, local e_{xy} maxima predate the formation of a new thrust imbricate within the pro-layer, which is concordant with the information deduced from the EDM. It follows that the communication or the ability to transfer strain between fore-thrusts within the pro-wedge and the retro shear-zone decreases with increasing distance between them. It is finally emphasised that the EDM and the strain histories of ramp segments provide complementary information and have to be viewed as such.

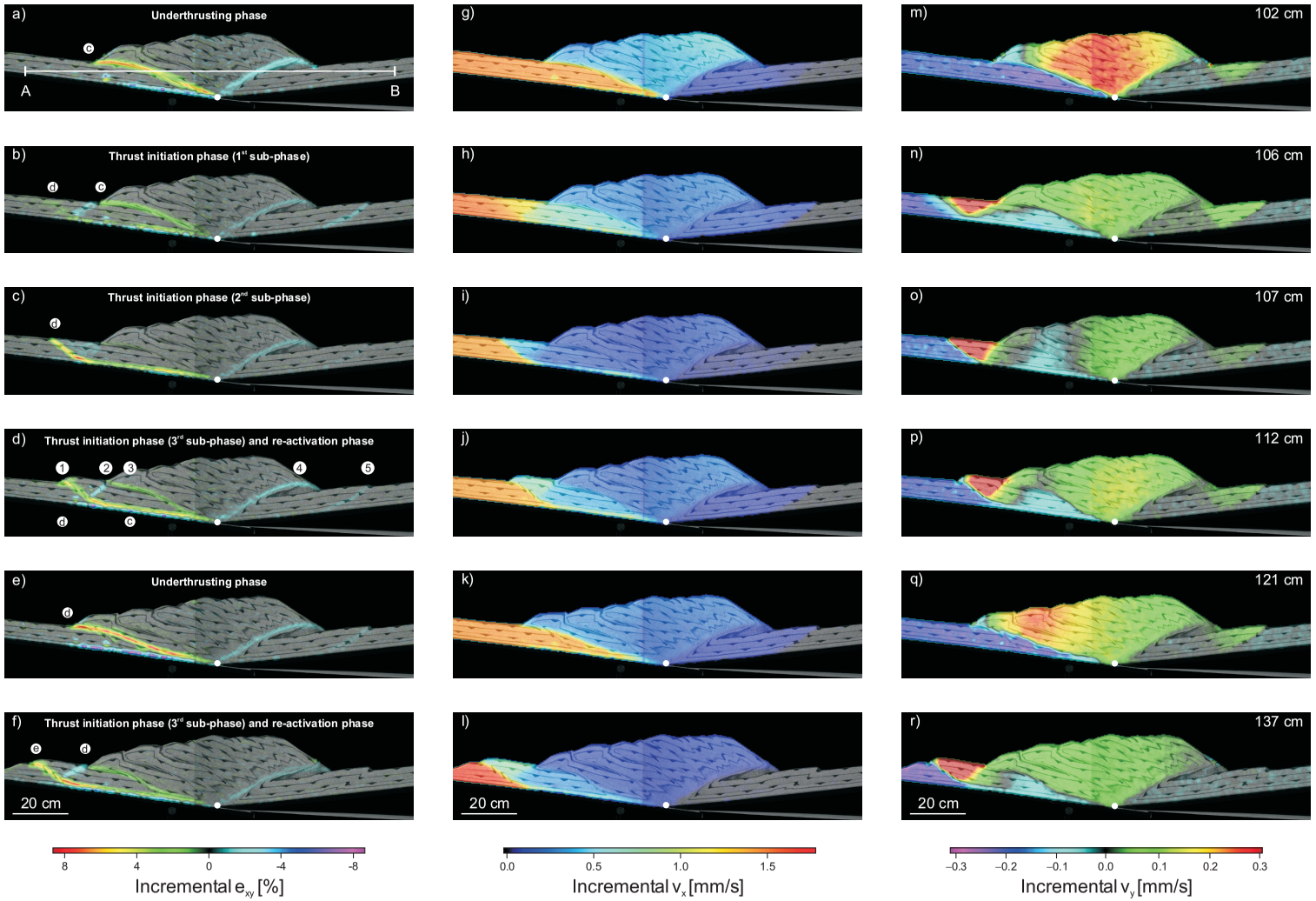

Figure 5.8: Sequential development of an accretion cycle. Columns from left to right show incremental e_{xy} and the respective horizontal and vertical component of the velocity field. Numbers on the right indicate *cm* of convergence. Interpretation of the e_{xy} pattern in terms of the accretion cycle is given. Evolution of profile AB in (a) is shown in figure (5.9). Labels ① to ⑤ in (d) refer to different thrusts and are explained in figure (5.9). Labels ⓑ to ⓔ denote successive thrust imbricates.

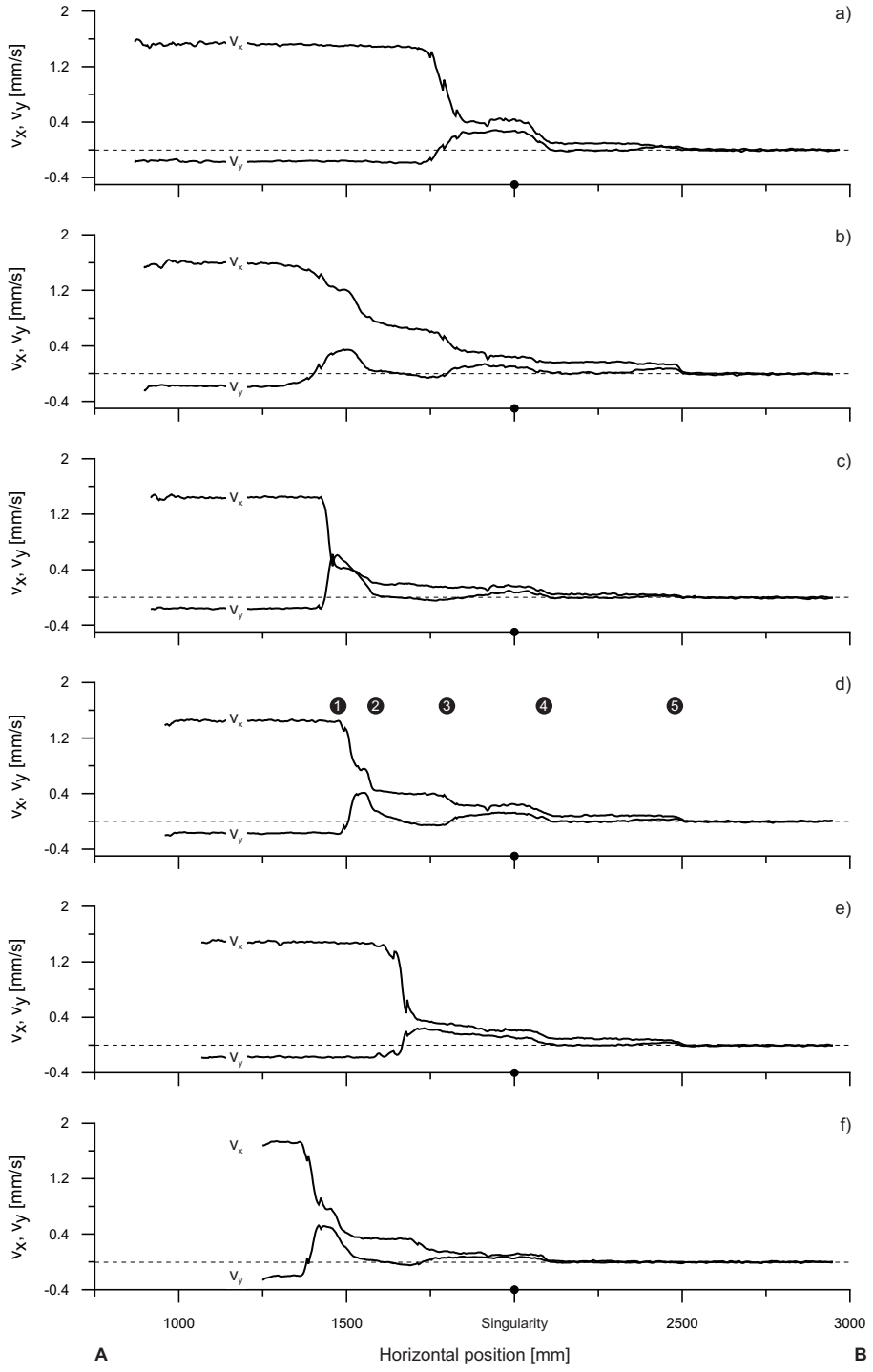

Figure 5.9: Evolution of the vertical and the horizontal component of the velocity field during an accretion cycle as derived from figure (5.8a). The initial plateau of v_x at $1.5\,mm/s$ is due to the velocity of the undeformed incoming layer, the negative values of v_y ($-0.3\,mm/s$) derives from the experimental setup, i. e., the sand-layer moves first downwards, as a response to the flexural deflection and is than tectonically uplifted. Note changes of either v_x or v_y across thrusts. Labels: ① Forethrust within the pro-wedge, ② The respective backthrust, ③ Internal thrust, ④ Retro-shear zone and ⑤ Forethrust within the retro-wedge.

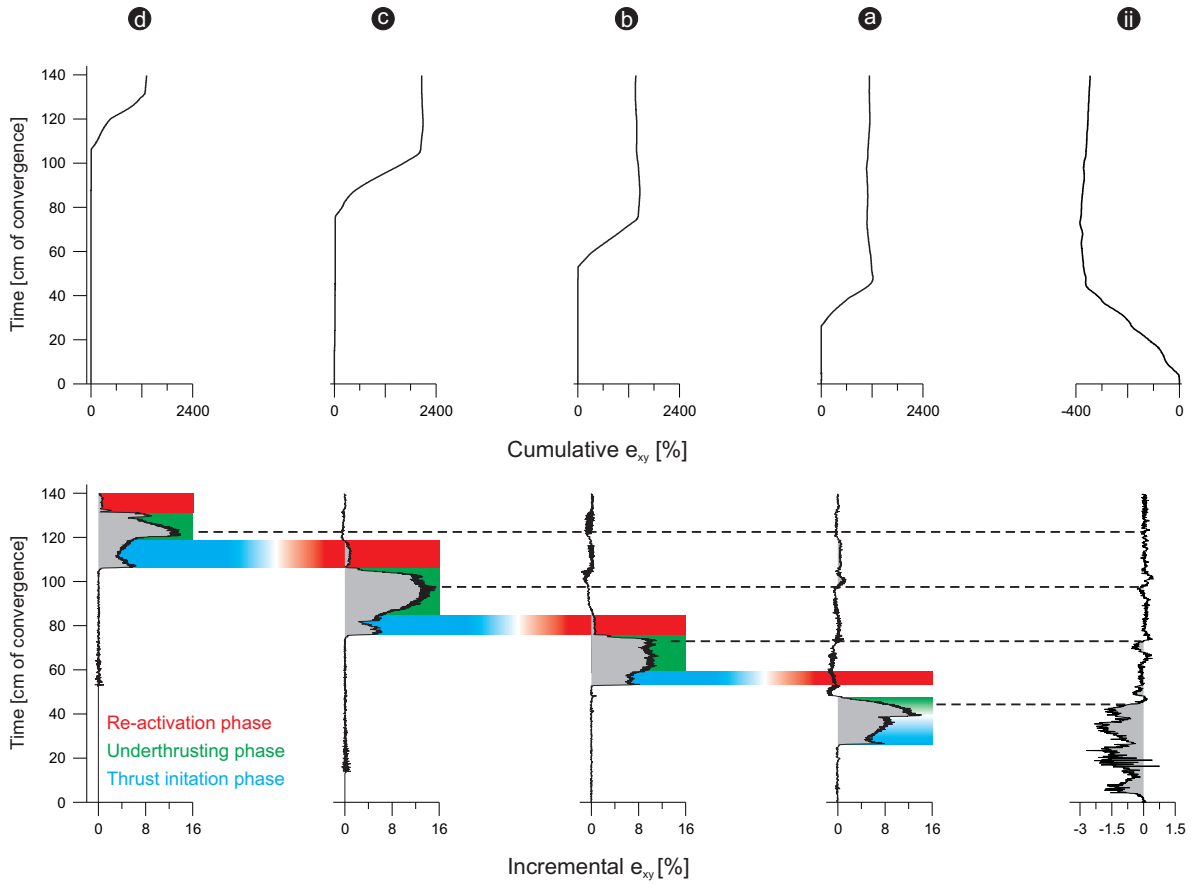

Figure 5.10: e_{xy} accumulation of forethrusts ⓐ to ⓓ and the retro-shear zone ⓘ. The phases of the accretion cycle are marked in coloured to visualise strain transfer. Note that the "communication" of the pro-wedge with the retro-shear zone follows a damped oscillation. Information in this figure is complementary to figure (5.7).

5.2 Experiments with other kinematic boundary conditions

A key observation is that neither changes of the mechanic stratigraphy nor the absence of flexure did inhibit the segmentation of the sand-wedges into a pro-wedge, an axial-zone and a retro-wedge (Fig. 5.11). With one exception all four bivergent sand-wedges showed the first three stages out of the four staged evolutionary pathway found for the reference experiment. Experiment 9.35, where the upper plate was made up of mortar, lacks stage II. The kinematic similarity between these four experiments is also evident from the time series data (Fig. 5.12). However, differences with respect to the accumulation and propagation of strain as well as the topographic evolution of the bivergent sand-wedges do exist and are outlined below.

Frontal accretion. Similar to the reference experiment, time series data from all four experiments show that the propagation of frontal accretion is composed of individual accretion cycles and to a lesser degree of footwall shortcuts (Fig. 5.12). The resulting overall trend of the lateral growth of the pro-wedge, is again best described by a power law. However, significant differences between the respective power law coefficients are observed (Table 5.1). The closest approximation between the experimentally derived

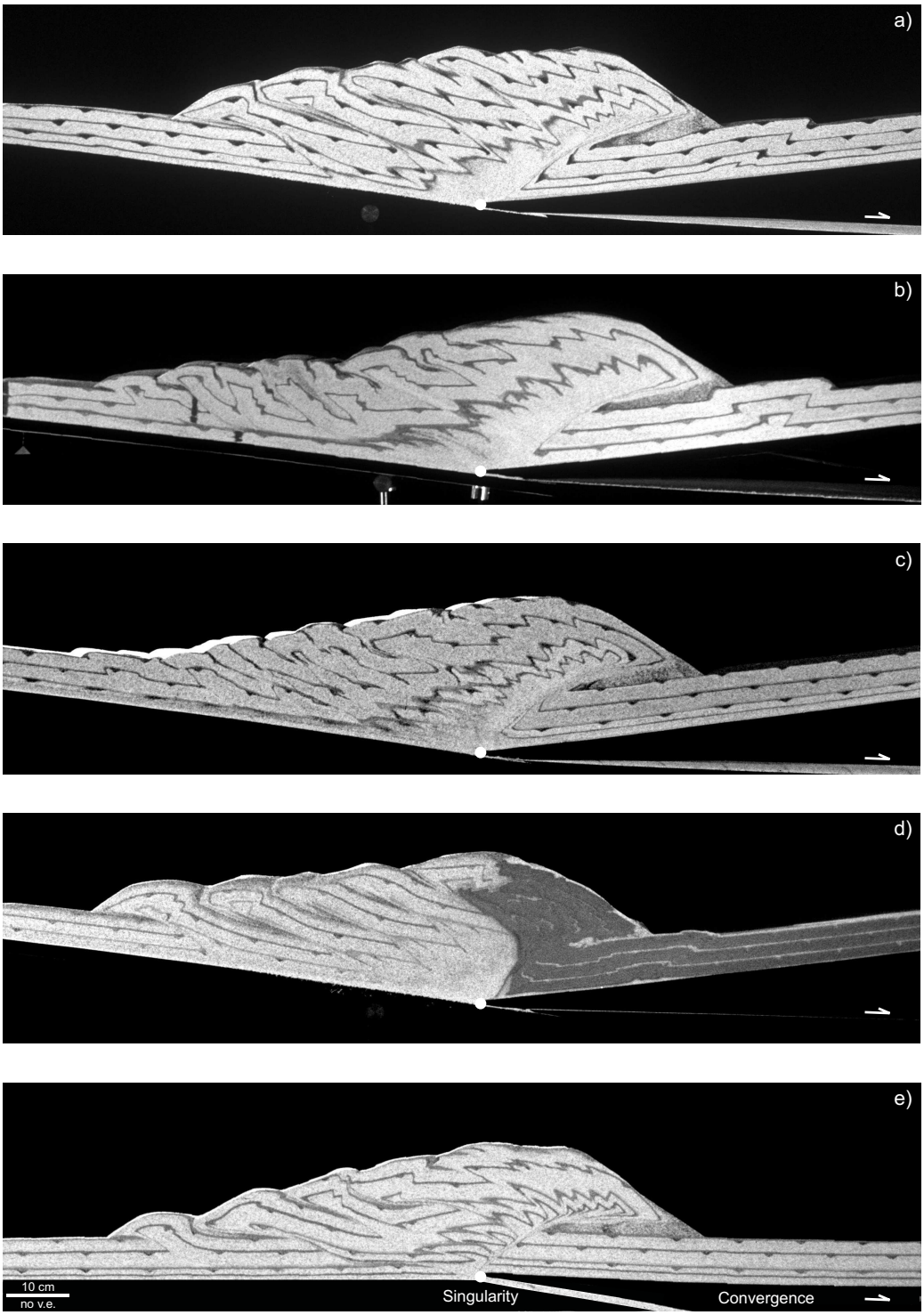

Figure 5.11: Photographic images of final stages of experiments: (a) Reference experiment 9.15; (b) Experiment 9.05; (c) Experiment 9.20; (d) Experiment 9.35; (e) Experiment 9.25; after 140 cm of convergence, except experiment (e), where convergence was 120 cm.

power law coefficients and the theoretically predicted value of 0.5 (Dahlen, 1990) is found in experiments, where two conditions are met. First, the respective mechanic stratigraphy is symmetric with regard to a horizontal symmetry plane. Second, no changes of the mechanic stratigraphy across the singularity do occur (vertical symmetry plane). Both conditions are satisfied in experiment 9.15 and 9.20. In the remaining experiments (9.05, 9.25, 9.35), where only one boundary condition is given, significant deviations of the respective power law coefficients from the theoretically predicted value are observed (Table 5.1). However, the largest difference between the theoretical value and the experimentally derived one was found for experiment 9.35, where the upper plate was made up of mortar. This might indicate that a strength contrast across the singularity has a stronger influence on the propagation of deformation within the pro-wedge, than changes of the mechanic stratigraphy with respect to the number and vertical distribution of weak layers. An experiment, in which both boundary conditions are not provided, has not been carried out but would be due to be done.

The depth to the detachment determines the number of thrust imbricates (Table 5.1). Experiments without an internal detachment, i. e., the depth to detachment is $6\,cm$ show five imbricates (9.15, 9.35) whereas experiments with an internal detachment, i. e., the depth to detachment is $4\,cm$ result in eight imbricates (9.05, 9.20). In experiment 9.25 a cyclic change of the position of the detachment was observed. The detachment was first initiated as a basal detachment, i. e., above the conveyor belt and jumped during the following accretion cycle to the internal weak-layer.

The spacing of frontal accretion, which describes how far deformation propagates into the foreland (Fig. 5.12), remains fairly constant throughout the experiments. If however, the depth to the detachment decreases as in experiment 9.20 and 9.25, the respective spacing decreases accordingly (Fig. 5.12). Interestingly, experiments where the basal detachment of frontal accretion is located above the conveyor belt show a higher variability in spacing, than those where the respective detachment is located in the glass-bead layer (Table 5.1).

Contrary, the wavelength, which is the time expressed in convergence between two consecutive thrust initiation events, varies within and between experiments and is thus more sensitive to the parameters tested. As a measure of this variability, the sample standard deviation of the wavelength of frontal accretion (s_{fw}) was calculated for all experiments. It is highest for experiment 9.25, which agrees with the observation of a changing depth to the detachment. s_{fw} is significantly lower for the remaining three experiments and shows a positive correlation with the number of weak layers (Table 5.1). Experiment 9.35 deviates from this trend and illustrates thus the influence of a strength contrast across the singularity on the propagation of deformation within the pro-wedge.

Basal accretion. During experiments, with either one or two internal glass-bead layers, decoupling of the upper from the lower sand-unit initiated after $\sim 40\,cm$ of convergence. Coeval to frontal accretion above the glass bead-layer the sand layer beneath it was detached from the one above and transferred towards the axial-zone. Here beneath the base of the pro-wedge duplexes were formed, continuously stacked, and finally uplifted in the hangingwall of the retro shear-zone. The initiation, formation, stacking and translation of these duplexes is referred to as basal accretion. In contrast to the very regular propagation of frontal accretion, basal accretion is more irregular in terms of its wavelength and its spacing (Fig. 5.12). The respective variability expressed in the sample standard deviation of the wavelength (s_{bw}) was as well calculated for all experiments. It emerges that s_{bw} is generally higher than s_{fw}. Also, the range of the latter (0.37) is nearly a third of the former (0.97) and suggests that basal accretion, as opposed to frontal accretion, is more sensi-

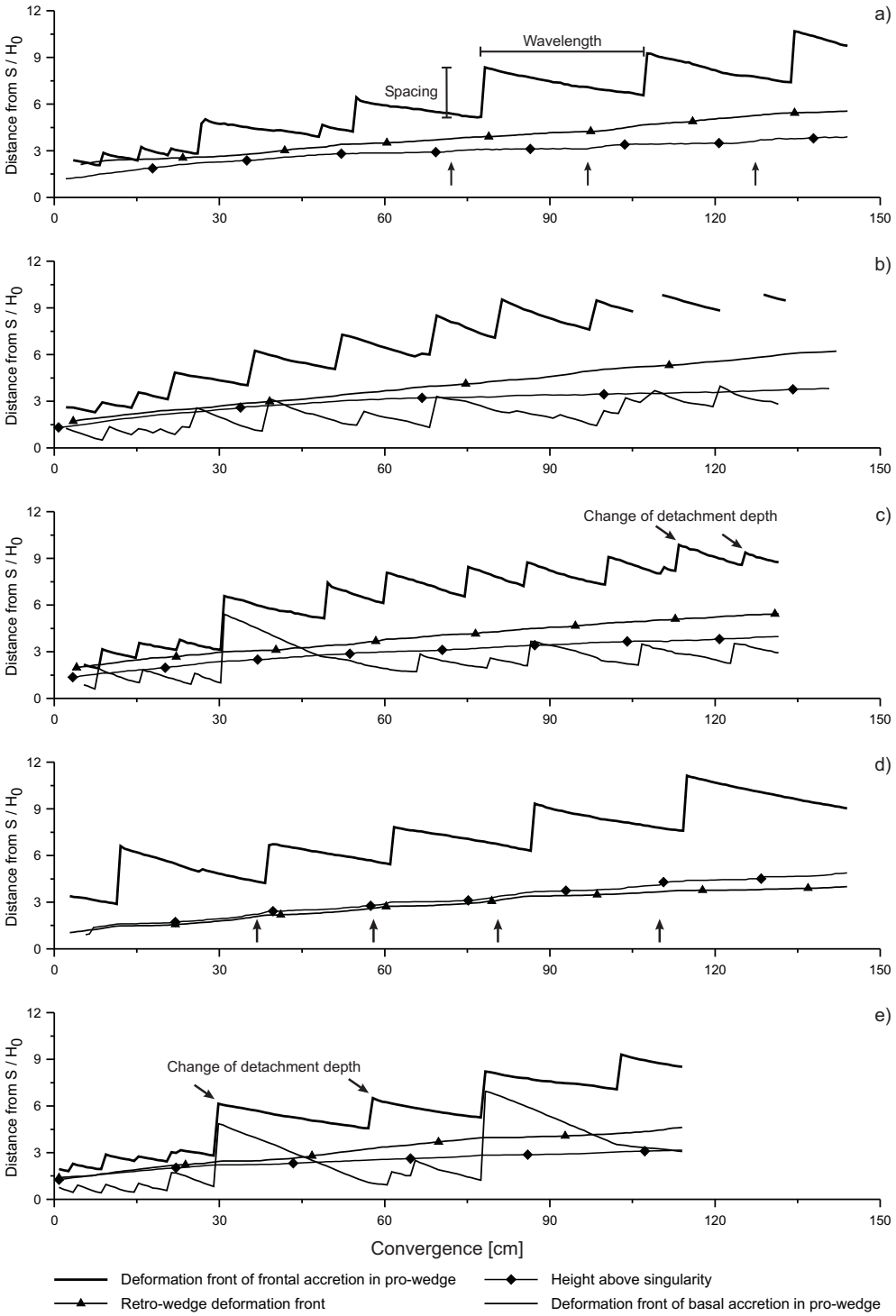

Figure 5.12: Evolution of geometric parameters taken from the digital images at every 1.5 *cm* of convergence. (a) Reference experiment 9.15; (b) Experiment 9.05; (c) Experiment 9.20; (d) Experiment 9.35; (e) Experiment 9.25. Arrows in (a) point to times of accelerated vertical growth, which predate the formation of a new thrust imbricate within the pro-layer. Arrows in (c) and (e) indicate changes of the depth to the detachment. Note the associated change of the thrust spacing.

Experiment Observations	9.15	9.35	9.05	9.20	9.25 *
Flexure	✓	✓	✓	✓	∅
Number of weak layers	0	0	1	2	1
Frontal accretion in retro-wedge	✓	✓	✓	∅	∅
Number of thrusts in pro-wedge after 140 cm of convergence	5	5	8	8	4
Sample standard deviation of wavelength of frontal accretion† s_{fw}	0.13	0.19	0.15	0.30	0.50
Sample standard deviation of spacing of frontal accretion† s_{fs}	0.15	0.15	0.07	0.09	§
Sample standard deviation of wavelength of basal accretion s_{bw}			0.47	0.90	1.44
Power law equation of lateral growth of pro-wedge $y_L =$	$0.79t^{0.48}$	$1.80t^{0.32}$	$1.06t^{0.44}$	$0.80t^{0.50}$	$0.97t^{0.43}$
Coefficient of determination $R^2_L =$	0.88	0.76	0.89	0.90	0.82
Power law equation of height above singularity $y_H =$	$0.85t^{0.29}$	$0.48t^{0.42}$	$1.03t^{0.26}$	$0.76t^{0.33}$	$1.00t^{0.23}$
Coefficient of determination $R^2_H =$	0.97	0.96	0.97	0.99	0.97
Out-of-sequence displacement (OOSD) index	0.62	3.95	3.73	8.1	0.46
Length ratio of pro-/ retro-wedge	2.82	2.47	3.03	2.75	1.82

* Only 120 cm of convergence.
† Without footwall shortcuts.
§ Not determined because of cyclic change of detachment depth.

Table 5.1: Summary of experimentally derived results – 1^{st} experimental series.

tive to the parameters tested (Table 5.1). Convergence intervals, where both accretion modes are either in or out of phase, are too short to be correlated over longer distances. It is finally pointed out that the height above the singularity provides a geometric envelope for basal accretion (Fig. 5.12).

Topographic evolution. Similar to the reference experiment, the topography of all four experiments consists of two domains: the first that comprises the pro-wedge and shows discrete steps and the second that encompasses the axial-zone and the retro-wedge with a concentric growth pattern (Fig. 5.13). Despite this first order similarity, the shape and evolution of both domains differ between experiments. For three experiments (9.05, 9.25, 9.35) examination of the topographic envelopes revealed a distinct topographic low within the respective pro-wedges. Accordingly, experiments which lack this topographic depression have a smoother topographic envelope. This is in agreement with a previous observation that the power law exponents of the lateral growth of the latter experiments are closer to the theoretically predicted value, than it is the case for the other three experiments (Table 5.1).

A closer analysis of the concentric growth pattern found within the second topographic domain shows that during experiments with basal accretion, this growth is nearly equidistant (Fig. 5.13). In experiments without basal accretion, the concentric growth pattern can be divided into periods of accelerated and slowed growth, whereas the latter are linked with the initiation of individual frontal accretion cycles (Fig. 5.13a, d). The relation between basal accretion and equidistant concentric growth of the second topographic domain can be tested with experiment 9.25. If the detachment is located above the conveyor belt, topographic outlines start to merge. A more equidistant growth pattern can be recognised during phases, where the detachment is located within the internal weak layer (Fig. 5.13e).

Incremental surface uplift of the four experiments shows a high spatio-temporal variability, similar to the reference experiment. Nevertheless, the key features identified previously can be clearly recognised: (i) two uplift domains; (ii) thrust traces, i. e., different phases of thrust activity associated with the accretion cycle; (iii) the temporal coincidence between maximum ISU within the pro-wedge and significantly

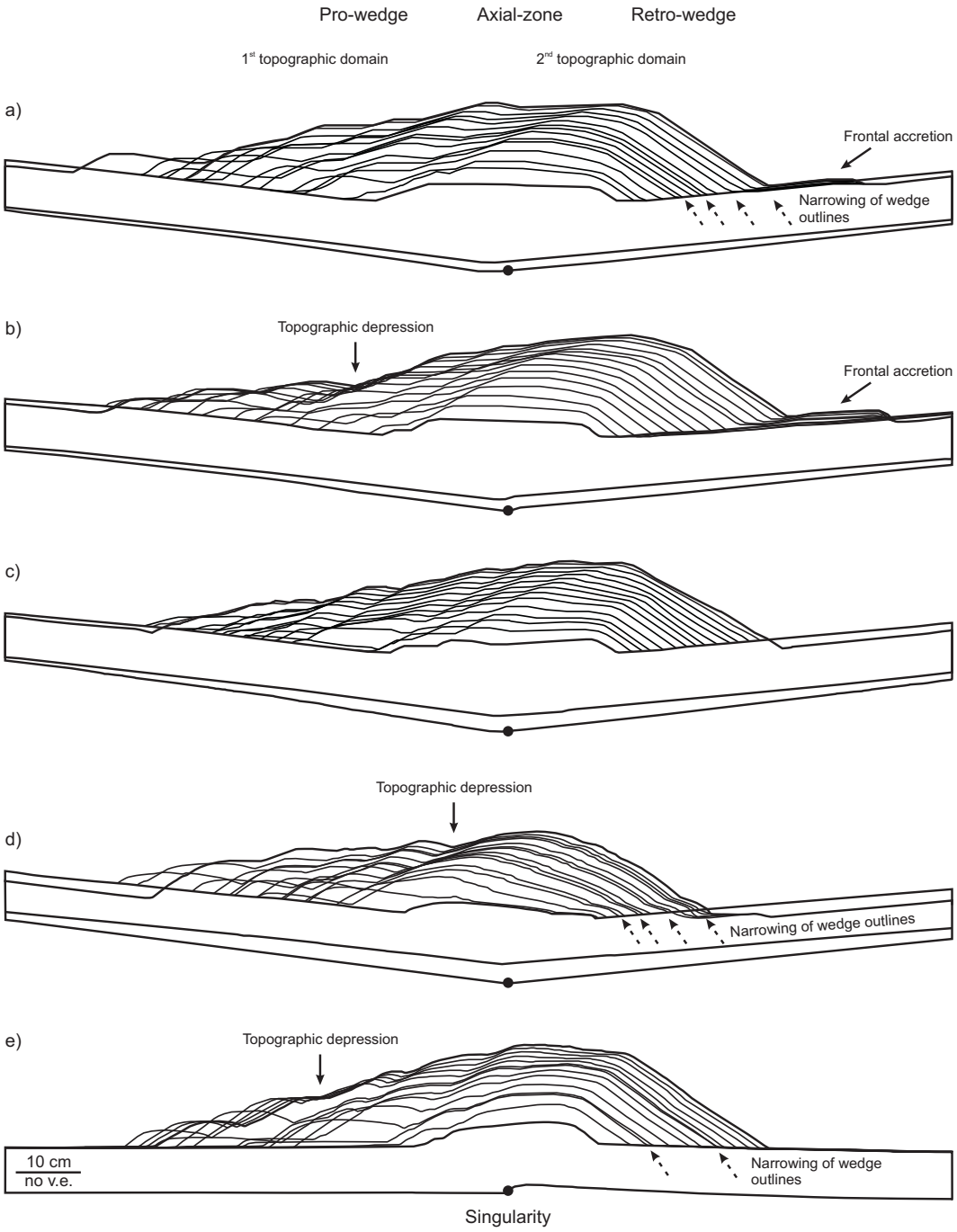

Figure 5.13: Topographic evolution of all experiments of the 1^{st} series. Outlines were taken at every $10\,cm$ of convergence. The first, i. e., after $10\,cm$ and the last, i. e., after $150\,cm$ of convergence outline are given in complete form, to indicate the magnitude of flexure. (a) Reference experiment 9.15; (b) Experiment 9.05; (c) Experiment 9.20; (d) Experiment 9.35; (e) Experiment 9.25. All experiments show two topographic domains: cyclic accretion within the pro-wedge results in distinct steps in topography, whereas continuous addition of pro-wedge derived material to the axial-zone and the retro-wedge leads to a nearly concentric growth. Experiments with an asymmetric mechanic stratigraphy show a marked topographic low within the pro-wedge. Dashed arrows indicate narrowing of wedge outlines, which are linked with thrust initiation phases.

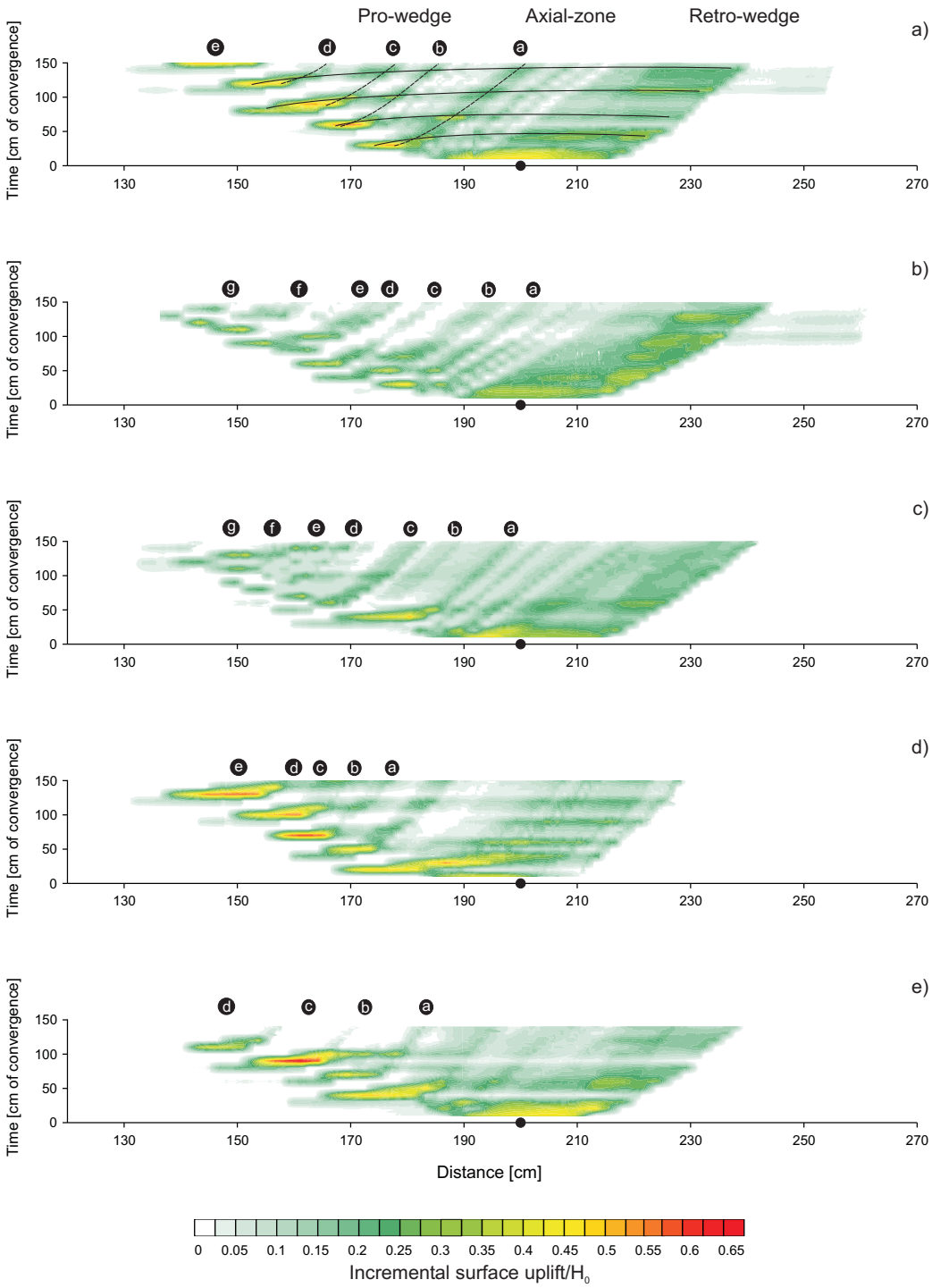

Figure 5.14: Incremental surface uplift map for all experiments of the 1st series. (a) Reference experiment 9.15; (b) Experiment 9.05; (c) Experiment 9.20; (d) Experiment 9.35; (e) Experiment 9.25. Interpretation of thrust traces (dashed lines) as well as surface uplift waves (bold lines) is only provided for (a), but can be recognised in all experiments. Labels ⓐ to ⓖ refer to forethrusts within the pro-wedge. Higher magnitudes of ISU within the pro-wedge of (a), (d) and (e) result from a deeper detachment level, i. e., 6 *cm*.

lowered ISU within the axial-zone and the retro-wedge and (iv) surface uplift waves associated with the accretion cycle (Fig. 5.14). The latter are most pronounced in experiment 9.35, which lacks basal accretion (Fig. 5.14d). In experiments with basal accretion (9.05, 9.20) ISU waves remain a very subtle feature (Fig. 5.14b, c). Both observations are thus concordant with the findings from experiment 9.25. If the detachment is located above the conveyor belt, i. e., only frontal accretion operates, a consecutive ISU wave can be traced. However, if the detachment is positioned within the internal weak layer, a respective surface uplift wave is hard to detect (Fig. 5.14e). It is finally highlighted that the ISU pattern does not mirror the accretion of individual duplexes.

Strain accumulation. Similar to the reference experiment, finite strain was calculated for each experiment (Fig. 5.15). The main structural elements such as the basal and the internal detachment, the retro shear-zone, individual thrust imbricates, duplexes as well as hangingwall shortcuts can be clearly identified. As recognised in the reference experiment the magnitude of retro shear is highest at the retro shear-zone, which separates lower plate from upper plate material and is thus again interpreted as long-lived. Back-thrusts intimately linked with the initiation of the flat-topped box anticlines accumulated only minor magnitudes of incremental strain and are therefore difficult to recognise in the finite strain images. A similar distribution of finite strain, as observed in the pro-wedge of the reference experiment, is found in all four experiments, i. e., cumulative e_{xy} magnitudes are highest for thrust imbricates located within the central part of the pro-wedge close to the topographic break, if present. On the other hand thrusts positioned either at the toe or at the top of the pro-wedge show significantly lower cumulative e_{xy} magnitudes (Fig. 5.15). Based on these observations a first order similarity in terms of strain accumulation and distribution between the reference and the experiments with varied kinematic boundary conditions is postulated.

However, if similar structures are compared between experiments, it emerges that different magnitudes of finite strain were accommodated. This is assigned to the respective kinematic boundary conditions and examples are provided below. Thrusts, which have a common depth to the detachment are characterised by similar finite strain magnitudes. In experiment 9.15 and 9.35, where this depth is $6\,cm$, the finite strain magnitudes are generally higher (Fig. 5.15a, d) than in experiment 9.05 and 9.20, where the depth to the detachment is only $4\,cm$ (Fig. 5.15b, c). This trend can also be recognised in experiment 9.25 (Fig. 5.15e). Here, finite strain magnitudes of thrust imbricates, which detach just above the conveyor belt ($6\,cm$) are higher than the respective magnitudes of thrust imbricates with an internal detachment level ($4\,cm$). The former magnitudes compare well with the ones derived from experiment 9.15 and 9.35, whereas the latter magnitudes are in a similar range as the ones from experiment 9.05 and 9.20. This dependence of finite strain magnitude on the depth to the detachment was found to be independent of the relative position of individual thrust imbricates within the pro-wedge.

Finite strain at the retro shear-zone is highest in experiment 9.05 and lowest in experiment 9.35. Interestingly, finite strain at the internal detachment is also highest for experiment 9.05 (Fig. 5.15b). In experiment 9.20 and 9.25 however, this internal detachment is difficult to recognise within the finite strain image (Fig. 5.15c, e).

Strain propagation and the thrust cycle. Similar to the reference experiment, the EDM provide a detailed insight in the spatio-temporal distribution of incremental e_{xy} for the experiments described in this section and the main structural elements such as: the initial pop-up, the retro shear-zone, individual thrust imbricates within the pro- and the

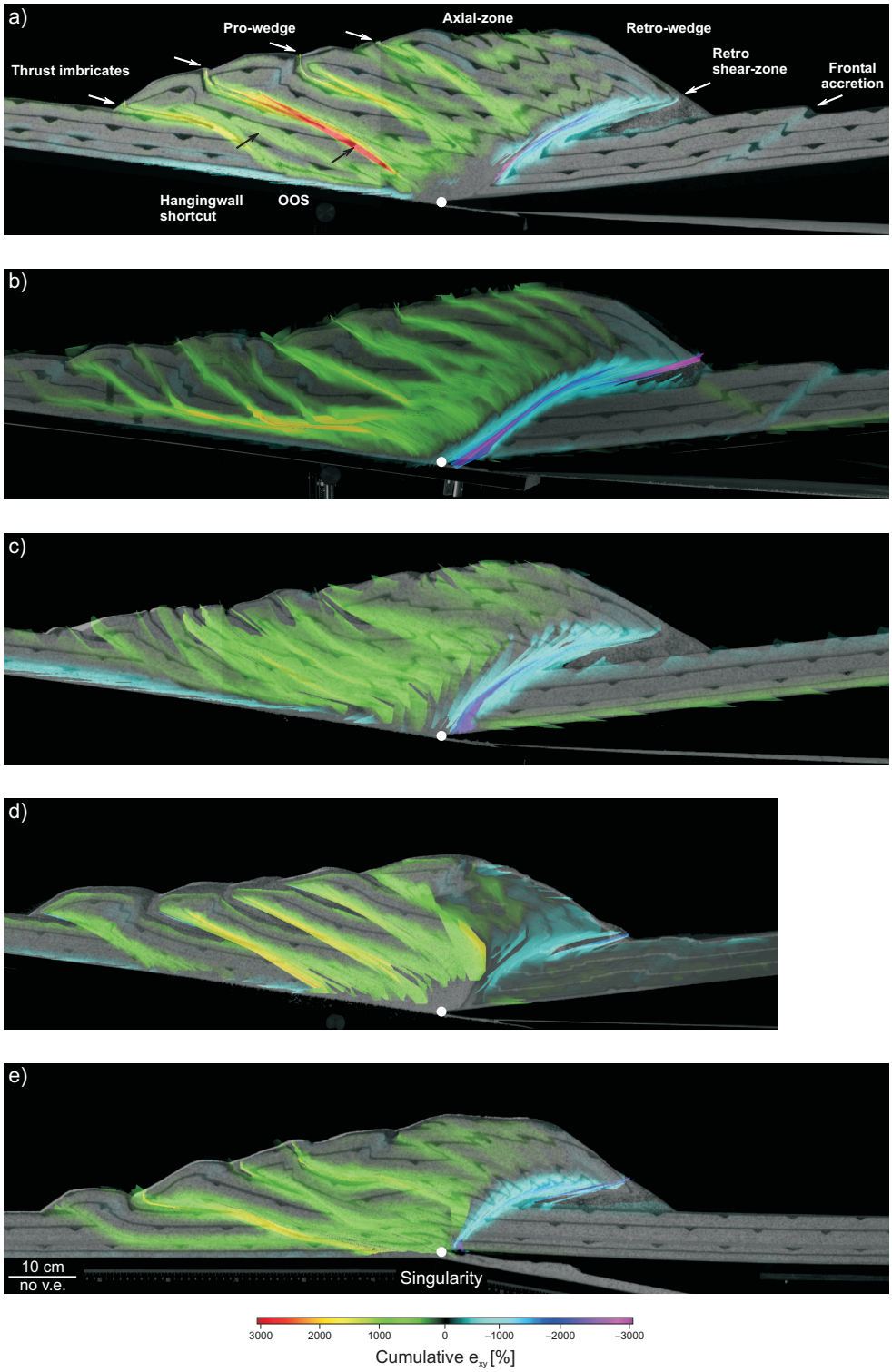

Figure 5.15: Finite e_{xy} after 140 cm of convergence. (a) Reference experiment 9.15; (b) Experiment 9.05; (c) Experiment 9.20; (d) Experiment 9.35; (e) Experiment 9.25 with only 120 cm of convergence.

retro-wedge as well as subtle features like backthrusts, footwall, and hangingwall shortcuts and out-of-sequence re-activation of thrust imbricates are clearly recognisable (Fig. 5.16). Even the late stage frontal accretion within the retro-wedge in experiment 9.35, which is not recognised in the finite strain image, leaves a very subtle trace in the EDM (Fig. 5.16c).

Furthermore, and most importantly, the regular strain pattern identified within the reference experiment and referred to as the accretion cycle, can be clearly observed for all experiments, although variations do exist. The latter can be related to the number of active backthrusts and the longevity of major thrusts. Especially, the time span and magnitude of out-of-sequence strain accumulation along thrusts varies between experiments. It is highest for the experiment 9.05 and 9.20 and is lowest for the experiments 9.25 and 9.35. Thus, in the former experiments, several structures accommodate e_{xy} at the same time, resulting in a smoothed EDM for which experiment 9.20 is a good example (Fig. 5.16b). Opposingly, the temporal overlap of e_{xy} accommodation by several structures is restricted to short episodes in experiment 9.25 and 9.35 (Fig. 5.16c, d). Note, that all experiments, except 9.20, show a pulsating e_{xy} accumulation along the retro shear-zone.

Similar to the reference experiment, the above observations are reflected in the e_{xy} histories of individual ramp segments of the fore-thrusts and the retro shear-zone (Fig. 5.17). Again, all three phases of the accretion cycle can be linked with the three maxima of incremental e_{xy}. The varying degrees of contemporaneous e_{xy} accumulation along several structures noted earlier can be clearly recognised as well. Within this respect, experiment 9.05 and 9.20 show the highest degree of overlap (Fig. 5.17a, b). It is furthermore evident from these graphs that the activity of the retro shear-zone within all experiments follows a pattern, similar to a damped oscillation. Inspection by eye of (Fig. 5.17) reveals that the magnitude of damping differs significantly between experiments and is assumed to be highest in experiment 9.20 (Fig. 5.17b) and lowest in experiment 9.25 (Fig. 5.17 d). e_{xy} maxima, which predate the formation of a new thrust imbricate within the prolayer show a shape, which are similar to a funnel, while using the terminology of well log analysis (Rider, 2000). Interestingly, the response of the retro shear-zone in terms of e_{xy} accumulation differs in dependence on the depth to the detachment (Fig. 5.17d). As outlined above, experiment 9.25 shows two cycles, where each cycle is composed of two accretion cycles, one with $6\,cm$ and one with $4\,cm$ detachment depth. During the former, the response of the retro shear-zone is similar to a funnel, during the latter, a box-like shape is found.

Out-of-sequence displacement. Frontal accretion in all experiments shows a pure forward-breaking or piggy-back thrust-sequence, although the corresponding displacement along each individual thrust is accumulated at several stages during wedge evolution. The result of this re-activation of older thrusts is termed out-of-sequence displacement. Based on the cumulative length evolution of individual thrusts, two end-member kinematic scenarios can be identified, between which all transitions are possible (Fig. 5.18). Thrusts, with only one phase of activity, are found in the reference experiment as well as in experiment 9.25 and 9.35 (Fig. 5.18a, e, d). However, careful examination of this figure reveals that the cumulative thrust length curves are made up of three segments. While the first segment is characterised by a gentle slope, the second segment shows a significantly steeper slope. The slope of the third segment approaches almost zero. This observation agrees with results derived from the analysis of the spatio-temporal distribution of e_{xy} (Fig. 5.17). Within this scenario, the first segment correlates with the postulated thrust initiation phase and the second segment with the underthrusting and the re-activation phase.

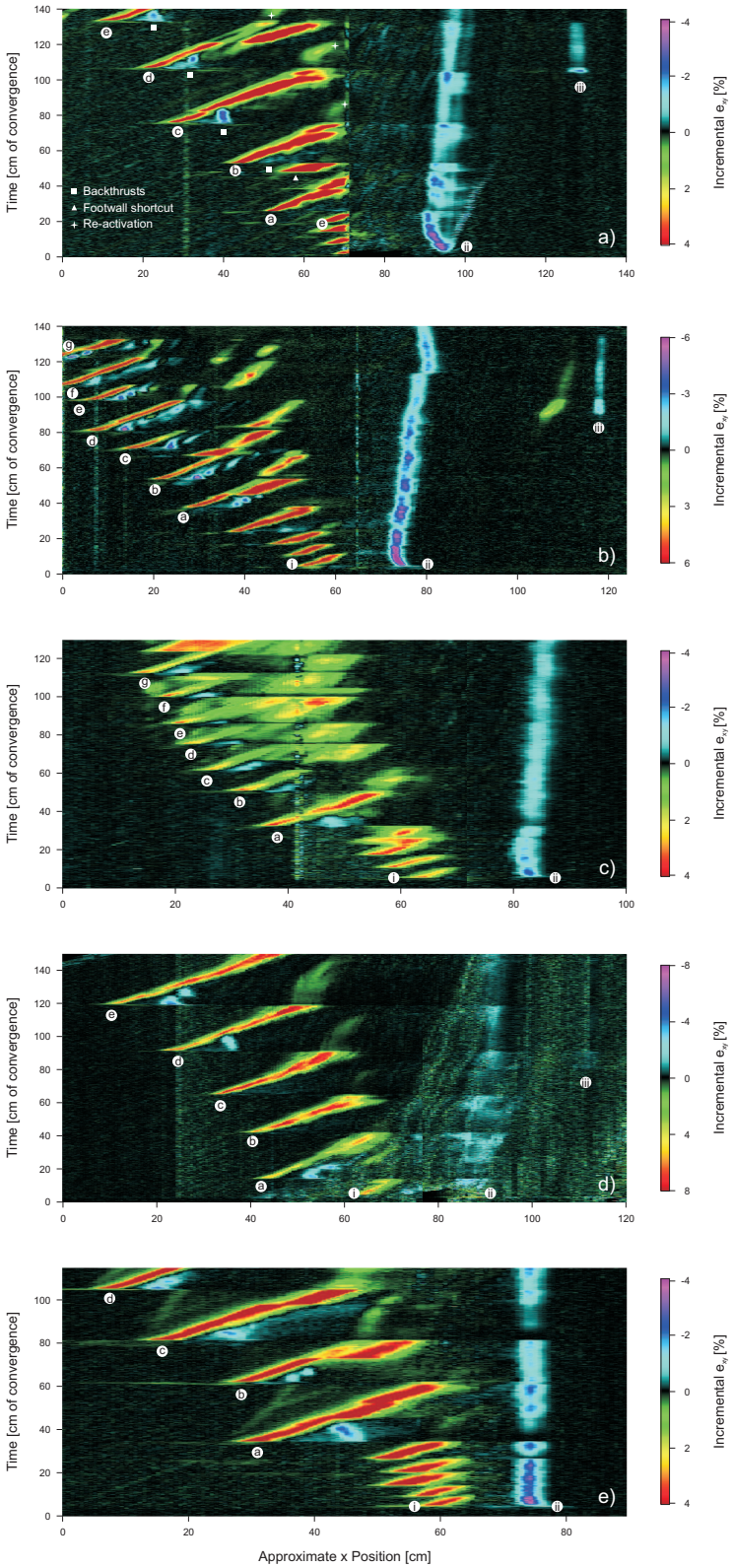

Figure 5.16: EDM for all experiments of the 1^{st} series. (a) Reference experiment 9.15; (b) Experiment 9.05; (c) Experiment 9.20; (d) Experiment 9.35; (e) Experiment 9.25. Labels ⓐ to ⓖ refer to forethrusts within the pro-wedge. ⓘ denotes the pro-shear of the initial pop-up, ⓘⓘ the respective retro-shear and ⓘⓘⓘ denotes the frontal accretion within the retro-wedge. The accretion cycle with its three phases can be recognised in all experiments. This figure is aimed at showing maximum details. Therefore strain magnitudes are not the same but similar. Positions of profile line with respect to the ramp segments of the forethrusts may vary within and between experiments. Changes of the magnitude may result, but the overall pattern is not affected. This figure provides complementary information to the following figure.

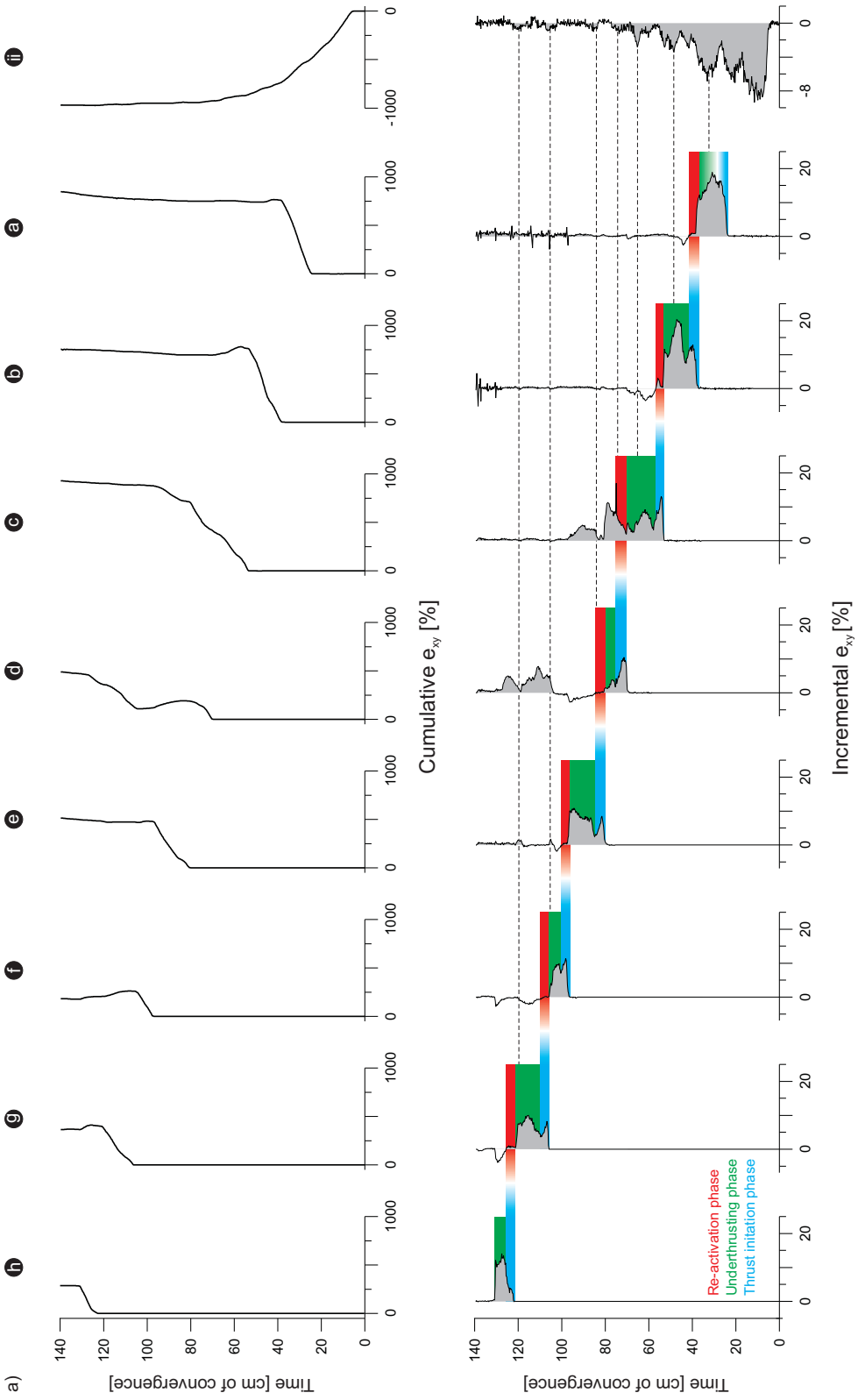
a)
Time [cm of convergence]
Cumulative e_{xy} [%]
Incremental e_{xy} [%]
Re-activation phase
Underthrusting phase
Thrust initation phase

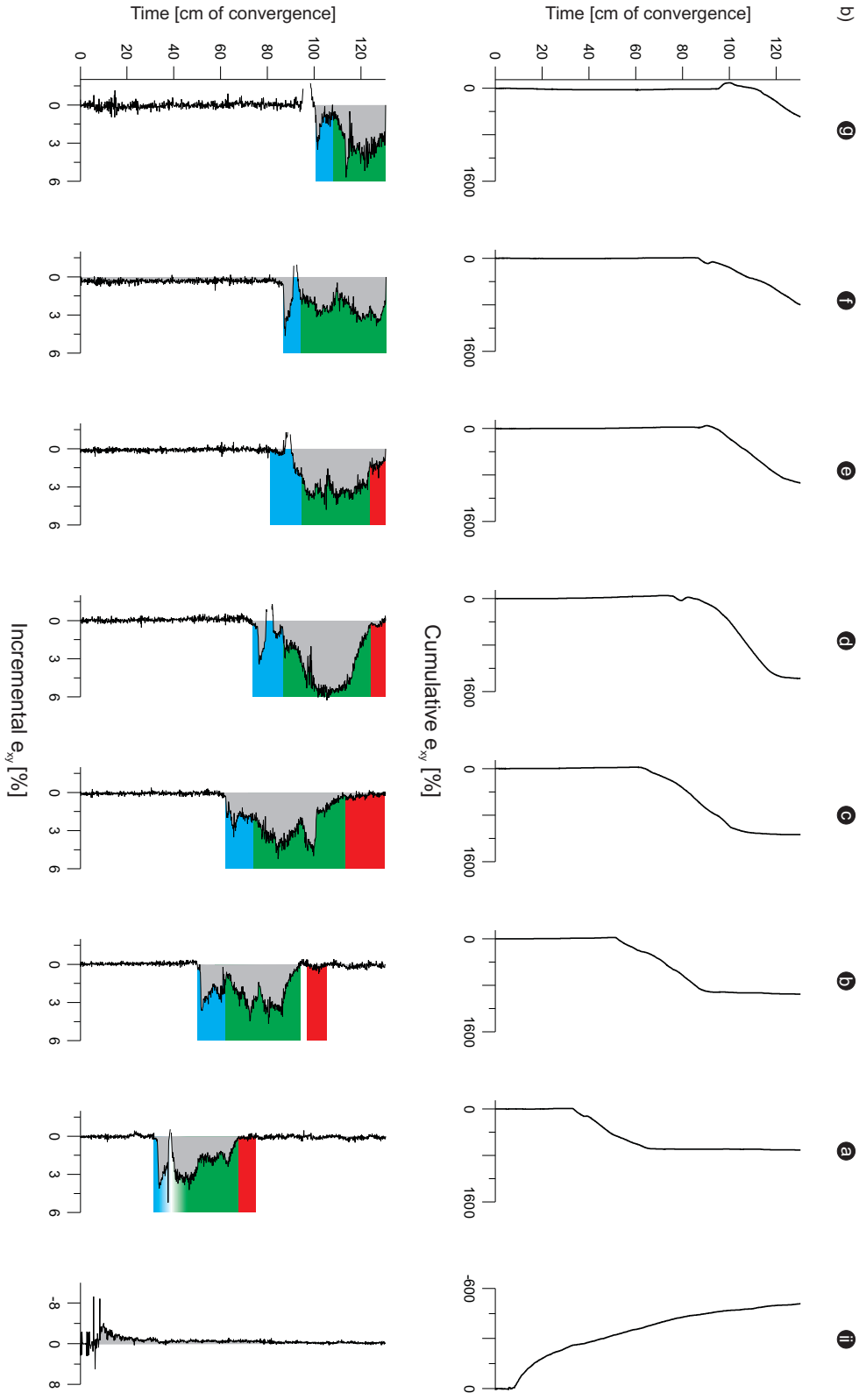
b)
Time [cm of convergence]
Time [cm of convergence]
Incremental e_{xy} [%]
Cumulative e_{xy} [%]
g
f
e
d
c
b
a
ii

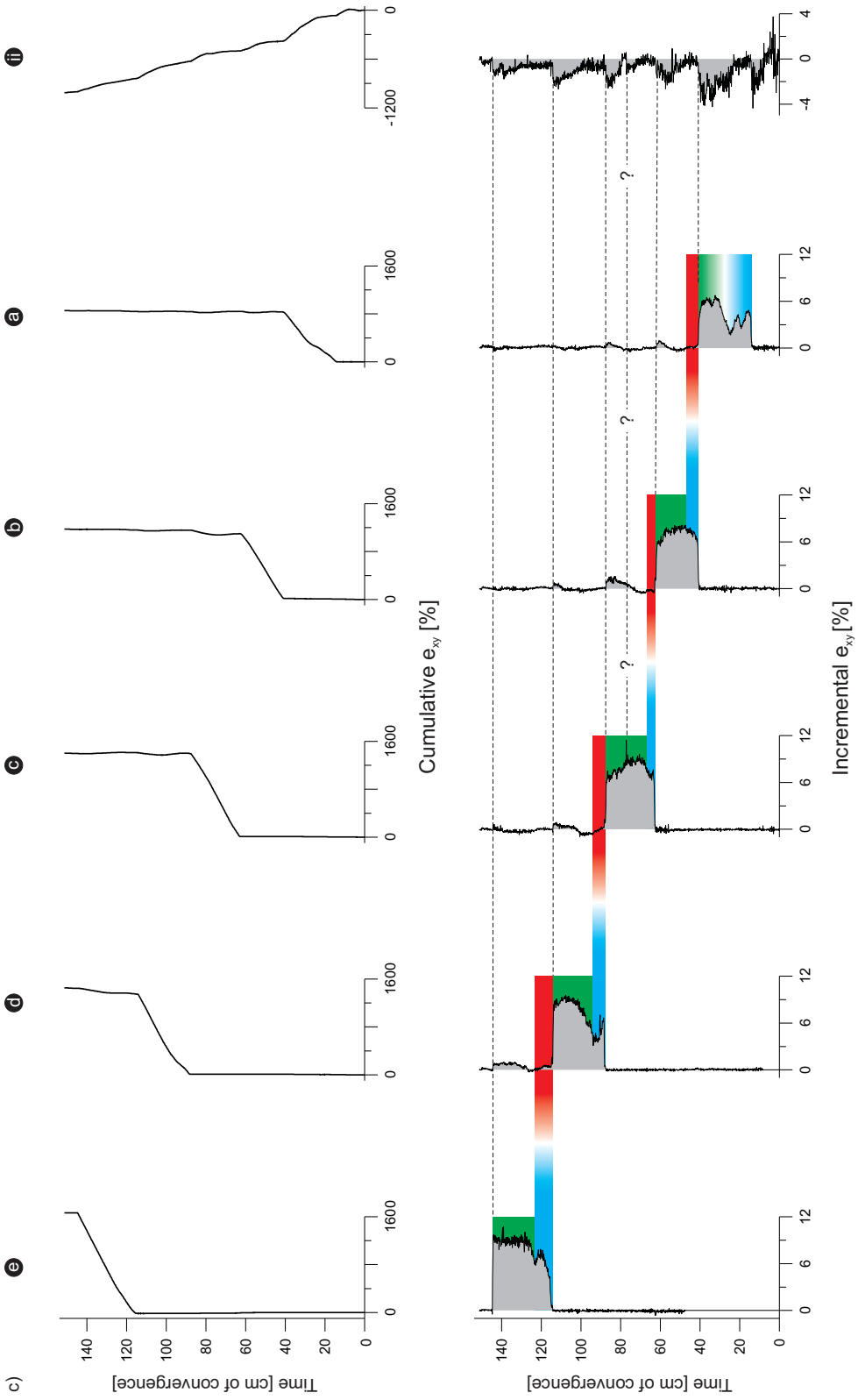
c)
Time [cm of convergence]
0
20
40
60
80
100
120
140
Cumulative e_{xy} [%]
Incremental e_{xy} [%]
e
d
c
b
a
ii
0
1600
-1200
12
6
4
-4
?

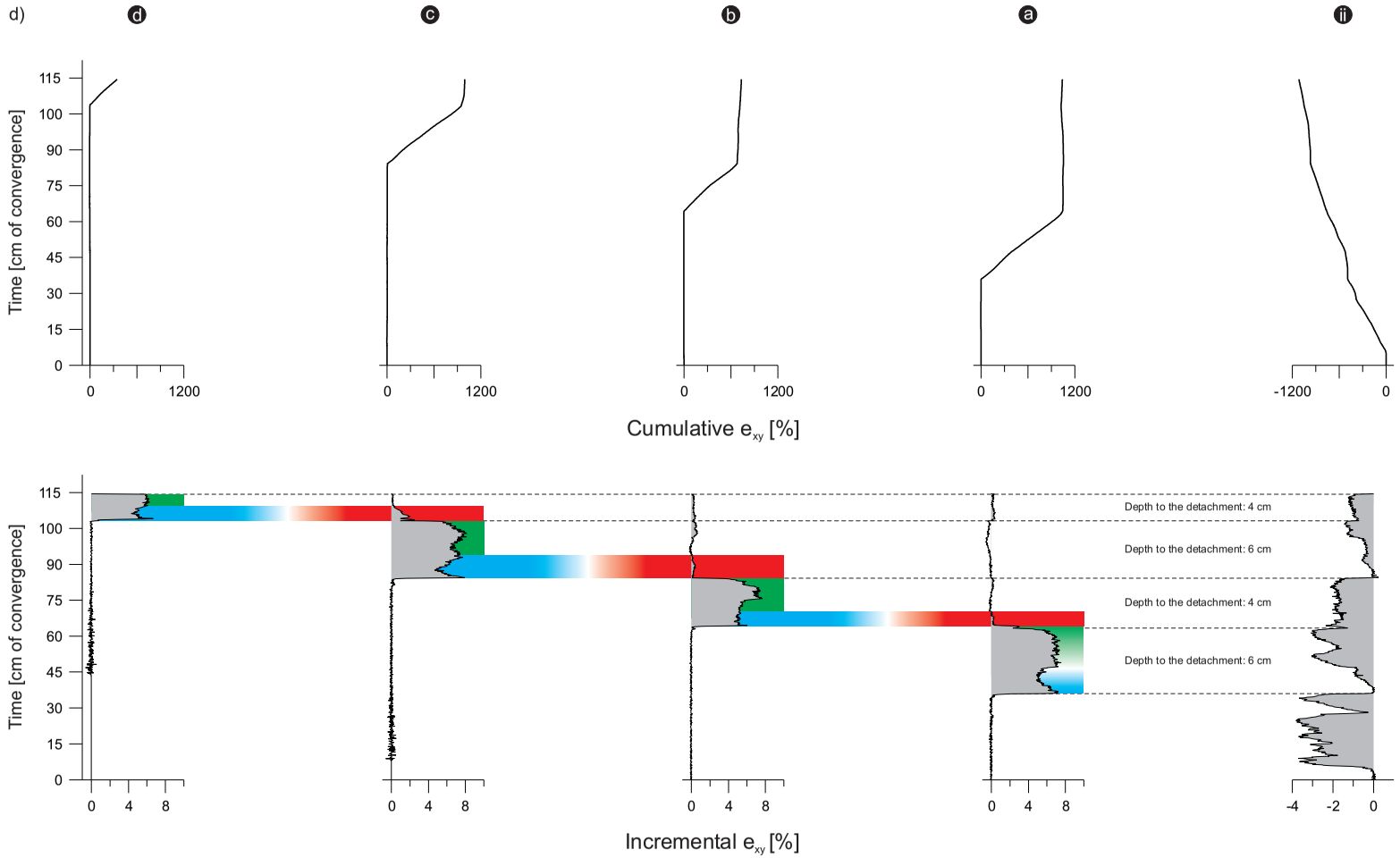

Figure 5.17: Strain accumulation of forethrusts within the pro-wedge ⓐ to ⓖ and the retro-shear zone ⓘⓘ. (a) Experiment 9.05; (b) Experiment 9.20; (c) Experiment 9.35; (d) Experiment 9.25. Letters in circles refer to forethrusts within the pro-wedge. Roman ii denotes the retro-shear zone of the initial pop-up. Coloured areas mark times of the three phases of an accretion cycle: blue – thrust initiation phase, green – underthrusting phase and red – re-activation phase. Each phase is associated with different peak values of e_{xy}. Dashed lines link pro-wedge deformation with the one of the retro-shear zone. Such a link is difficult to establish for experiment 9.20 (b), given the low amplitude accumulation of e_{xy} at the retro-shear zone. Magnitude of e_{xy} along the retro-shear zone decreases with increasing length of the pro-wedge and can be described by a damped oscillation. Experiment 9.25 (d) indicates that the response of the retro-shear zone depends on the depth to the detachment.

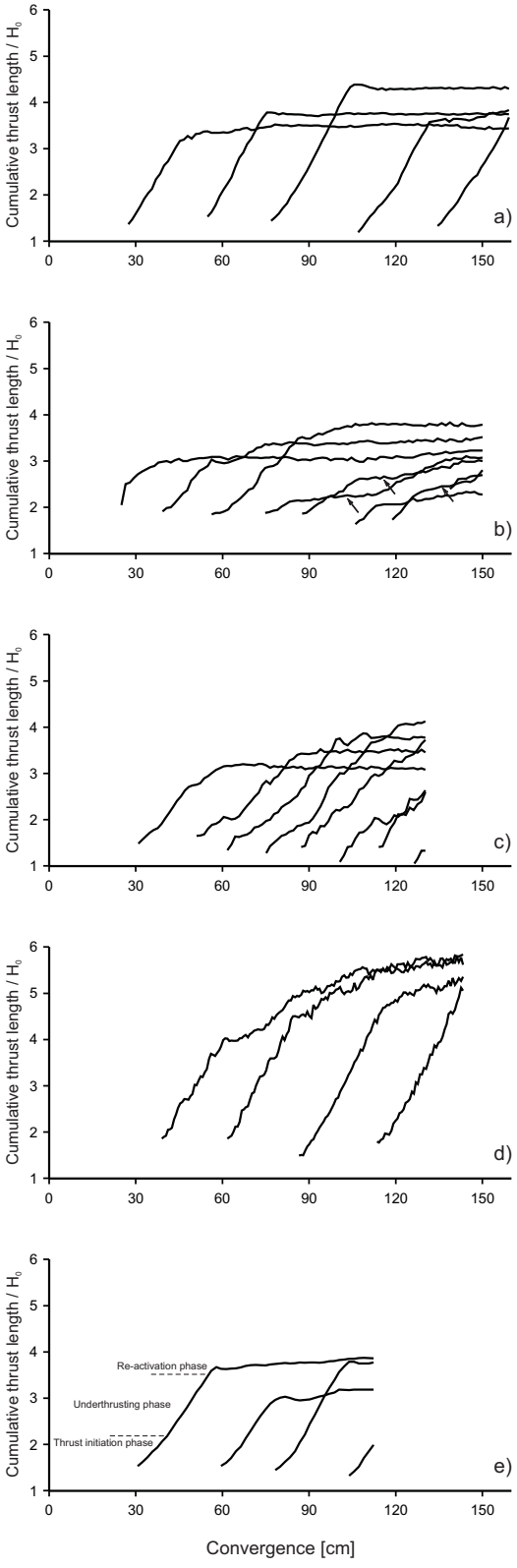

Figure 5.18: Cumulative thrust lengths of each thrust within the pro-wedge, taken at every 1.5 *cm* of convergence. (a) Reference experiment 9.15; (b) Experiment 9.05; (c) Experiment 9.20; (d) Experiment 9.35; (e) Experiment 9.25. Each curve consists of three segments, each with a different gradient. They correlate with the three phases of the accretion cycle. Note that some thrusts in (b) show a temporal offset between the underthrusting phase and the re-activation phase (arrow).

A slight difference of the cumulative length evolution is recognised for thrusts from experiment 9.05 and 9.20. They are characterised by two distinct phases of activity, separated by a period of quiescence. This is consistent with observations from the e_{xy} profiles (Fig. 5.17a, b), which indicate that the re-activation phase is temporally offset from the underthrusting phase. To quantify out-of-sequence activity, an out-of-sequence displacement index (OOSD) was derived, which is based on the magnitude of slip accumulated out-of-sequence. This OOSD index is highest for experiment 9.20 and lowest for the reference experiment (Table 5.1). The reader's attention is finally drawn to the observation that in experiment 9.05, 9.15, and 9.20 the third thrust accumulates the maximum finite displacement. Thus, finite displacement increases from thrust one to thrust three and decreases with later thrusts.

5.3 Discussion

5.3.1 Four-staged evolutionary model for bivergent sand-wedges

Deciphering the influence of kinematic boundary conditions, such as different mechanic stratigraphies and the degree of flexure on bivergent-wedge evolution was one of the key targets of this study. In order to address this issue, scaled 2D sandbox simulations were chosen. Confidence about the appropriateness of the selected setup is derived from the observation that all six key features of natural bivergent wedges (section 3.1)

were observed during experiments: (i) the asymmetry of the convergence geometry; (ii) the polarity of the mass-transfer; (iii) the bivergence of structures; (iv) the emergence of two sub-wedges, the pro-wedge with a low and the retro-wedge with a higher topographic gradient; (v) the dominance of deformation in the pro-wedge during early stages and migration of deformation into the upper plate during later stages of collision and (vi) the flexural downbending of the plates (Fig. 5.11).

All conducted experiments followed a similar four-staged evolutionary pathway: (I) initiation of a symmetric pop-up; (II) formation of a proto pro-wedge; (III) growth of the pro-wedge by frontal accretion and, in case an internal detachment layer was available, basal accretion and (IV) emergence of frontal accretion within the retro-wedge (Fig. 5.11, movies on DVD). The associated evolution of the lateral and vertical growth of the pro- and the retro-wedge is summarised in table (5.2) and agrees well with results from other sandbox and numerical simulations (Malavieille, 1984; Wang and Davis, 1996; Storti et al., 2000; McClay and Whitehouse, 2004; Willett et al., 1993; Beaumont et al., 1996; Naylor et al., 2005) and suggests thus reproducibility despite different setups and methodological approaches.

The proposed four-staged evolutionary model is also supported by observations from natural orogens. Uplift, folding and retroward translation of the initial pop-up might be envisaged as a crustal-scale backfold (Adrian Pfiffner pers. com.,(2003)). In the case of the Swiss Alps this backfold is marked by the Austroalpine nappes and is coeval with the onset of frontal accretion but remains active throughout the collisional history (Pfiffner et al., 2000). Based on balanced cross sections, Pfiffner et al. (2000) showed that frontal accretion preceded basal accretion, after collision started during the Late Eocene. This has also been documented for the Pyrenees (Beaumont et al., 2000) and for Taiwan (Lacombe and Mouthereau, 2002). Therefore, similar to the transition from stage II to stage III, as evidenced by experiments of this study, a certain load was needed to facilitate slip along deeper lying detachments. A late stage frontal accretion within the retro-wedge (transition from stage III to stage IV) is observed in the Pyrenees (Beaumont et al., 2000), the European Alps (Pfiffner et al., 2000), the German Variscides (Schäfer et al., 2000), and the Sunda Arc (Silver and Reed, 1988).

5.3.2 Strain transfer in bivergent wedges

Although we found that bivergent wedge evolution is very similar despite different kinematic boundary conditions, a likewise similarity with respect to the spatio-temporal distribution of strain was not expected, but observed. Indeed experimental results indicate that the accretion cycle with its three phases is a very robust process (Fig. 5.17). Therefore, a conceptual model of an accretion cycle is proposed (Fig. 5.19), which can be viewed as an extension of the one postulated by Gutscher et al. (1998) and Hoffmann-Rothe et al. (2004).

In addition, this conceptual model integrates and explains previously unrelated observations such as (i) the periodicity of thrusting (Cadell, 1888; Mulugeta and Koyi, 1992); (ii) the topographic evolution, especially the significant increase of the vertical growth rate at the rear of a wedge prior to the formation of a new thrust (Koyi, 1995; Storti et al., 2000; Naylor et al., 2005) and (iii) the cumulative slip evolution of thrusts (Storti et al., 2000; McClay and Whitehouse, 2004).

An exemplified accretion cycle might evolve as follows: during the thrust initiation phase, convergence is taken up by four thrusts, i. e., the forethrust, which defines the deformation front; the associated backthrust; an internal thrust, i. e., the previous deformation front and the retro shear-zone. The resultant incremental surface uplift is highest above the ramp segment of the forethrust and lowest above the retro shear-zone.

Stage	Distribution of deformation	Uplift of axial-zone and retro-wedge	Symmetry of bivergent sand-wedge
I*	Pop up	High	Symmetric
II†	Pro-wedge: high frequency thrust nucleation close to the singularity	High, but starts to decrease	Asymmetric
III§	Pro-wedge: low frequency thrust nucleation far from the singularity	low	Increase of asymmetry
IV‡	Pro-wedge: low frequency thrust nucleation far from the singularity Retro-wedge: frontal accretion	low	Asymmetric, but symmetry increases

Note: Bivergent wedge evolution has been described with different sequences of stages as indicated below.
* Corresponds to stage 1 in Storti et al. (2000) and stage 1 in Willett et al. (1993).
† Corresponds to stage 1 in Storti et al. (2000) and stage 2 in Willett et al. (1993).
§ Corresponds to stage 2 in Storti et al. (2000) and stage 2 in Willett et al. (1993).
‡ Corresponds to stage 3 in Willett et al. (1993).

Table 5.2: Summary of key characteristics of bivergent wedge evolution (Inspired by Storti et al. (2000)).

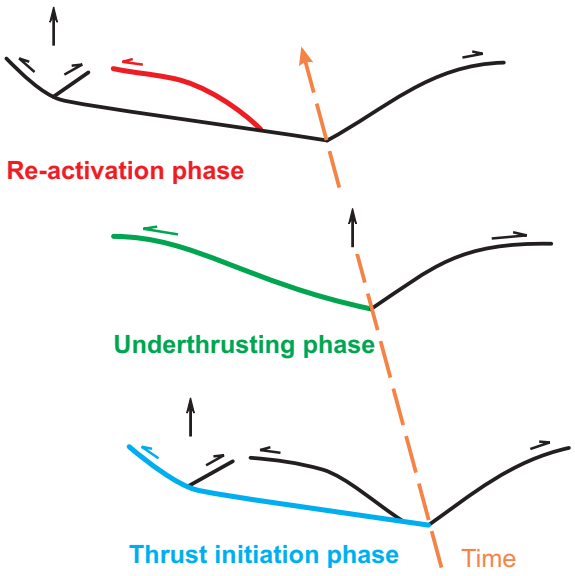

Figure 5.19: Conceptual model of an accretion cycle. The three phases thrust initiation, underthrusting and re-activation phase are colourcoded with respect to the forethrust. Vertical arrows indicate locations of maximum ISU. The accretion cycle is associated with a strain and a ISU wave. Both are initiated at the toe of the pro-wedge and migrate through the entire bivergent wedge until the retro-shear zone is reached. The phase within an accretion cycle controls thus the timing, location and magnitude of deformation and surface uplift.

In the following underthrusting phase, the forethrust evolves from a flat-ramp, via a ramp toward a ramp-flat geometry. The latter geometry is therefore similar to the one of the retro shear-zone (Fig. 5.14). Thus, the asymmetry associated with the thrust initiation phase is abandoned in favour of a more symmetric geometry during the late stages of the underthrusting phase. Thereby, the entire sand-wedge shortens horizontally and grows vertically. At the same time, a surface uplift wave, which mirrors locations of high e_{xy} accumulation, migrates through the entire wedge until it reaches the retro shear-zone.

During the third phase, i. e., the re-activation phase, deformation propagates outward into the pro-layer to form a new flat-topped box anticline and a new accretion cycle commences. The forethrust under consideration is now located in the hangingwall of the newly formed forethrust. This implies that the third phase of an accretion cycle is coeval with the first phase of the following accretion cycle. Strain transfer between two successive forethrusts can therefore not be considered as abrupt, i. e., one thrust is "switched" off while the other is "switched" on. Instead, strain is transferred gradually, i. e., the decay in activity of a forethrust is simultaneous with the increasing activity of the newly formed one (Fig. 5.16, Fig. 5.17). Thus, e_{xy} is not only partitioned in space but also in time. Thereby, the magnitude of

e_{xy} taken up by each thrust depends on its relative strength, which changes predictably through time, as outlined below (Fig. 5.20).

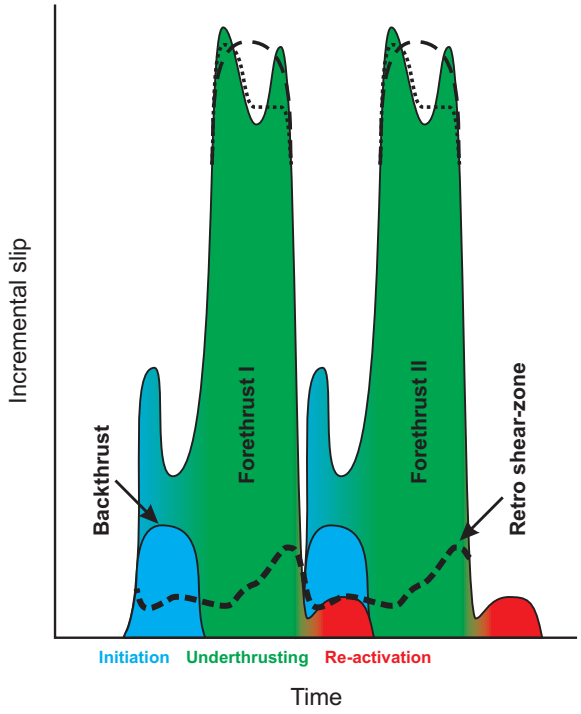

Figure 5.20: Incremental e_{xy} (slip) accumulation for all thrust, which are active during two accretion cycles. Magnitudes were taken from experiment 9.15. Phase within accretion cycle determines thus the location and magnitude of strain and slip accumulation. Therefore, strain and slip are partitioned in time and space. Note different peak scenarios for the underthrusting phase of two consecutive forethrusts.

Initiation of a thrust is associated with the successive formation and growth of isolated precursor structures, i. e., small-scaled shear zones (Nicol et al., 2002; Crider and Peacock, 2004). At the same time individual grains re-arrange and the porosity decreases significantly as evidenced by ring-shear measurements (Mandl et al., 1977; Lohrmann et al., 2003; Adam et al., 2005). This leads to an increase of the resistance to slip, since more grain boundaries are in contact with each other (strain hardening). The resultant strain accumulation is low. Coalescence of these small-scaled shear zones during the underthrusting phase results in a thoroughgoing shear zone with a flat-ramp geometry. Grains are now decompacted and more preferentially orientated with respect to the shear direction and slip accumulation is promoted (strain softening). However, the continuous transfer of the thrust under consideration towards the singularity, in conjunction with an increasing load upon this thrust, leads to its final locking during the re-activation phase. The respective e_{xy} magnitudes are low.

Given that e_{xy} accumulation along the retro-shear zones mirrors this evolution (Fig. 5.17) we postulate that the entire bivergent wedge is subjected to a strain hardening – strain softening cycle. Thus, during the thrust-initiation phase the wedge is "strain softest", but with continued convergence successively strengthened. At the very final stage of the underthrusting phase, the wedge is assumed to be "strain hardest". This results in a temporal dependence of the magnitude of strain accumulation for individual thrusts, although brittle failure by itself is independent of time (Byerlee, 1978). The accretion cycle is therefore considered as an internal clock of wedge-scaled deformation.

Differences between experiments with respect to the duration and magnitude of individual phases relate either to (i) the exact position of the profile line from which e_{xy} data were taken; (ii) the depth to the detachment and (iii) the number of degrees of freedom (section 5.3.3). It is emphasised that the change of the geometry of the deformation front from a flat-ramp, via a ramp toward a ramp-flat, mirrors the tripartite evolution of the accretion cycles (Fig. 5.8). This relation has lead Hoffmann-Rothe et al. (2004) to propose that the southern Chilean margin at 36° S is in a thrust initiation phase, but at 39° S it is in an underthrusting phase. Additionally, we have shown that the cumulative length evolution of thrusts reflects the three phases of the accretion cycle as well and can thus be used to constrain the latter, if strain monitoring techniques, such as PIV, are not available (Fig. 5.18, section 5.2).

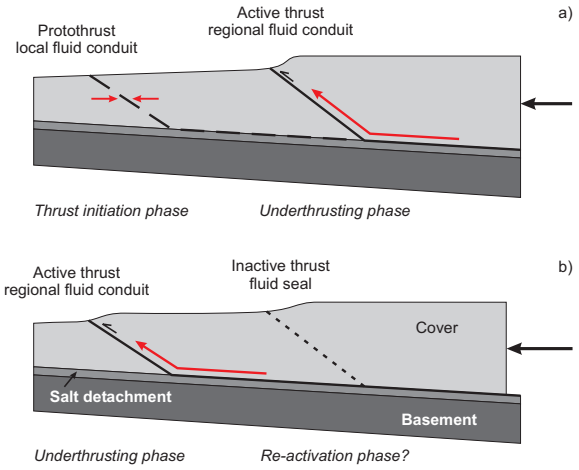

Figure 5.21: Relation of microfracture phase 1 (a) and 2 (b) with thrust development and main fluid-source (red arrows). Interpretation with respect to the conceptual model of an accretion cycle is given. Modified after Travé et al. (2000).

The above postulated kinematic model of an accretion cycle derives further support from a variety of field studies. Micro-structural work in the Appalachian fold and thrust belt has led Wojtal and Mitra (1986) to conclude that the emplacement of a thrust sheet generates an array of mesoscopic faults beneath it. These fault-bounded blocks are displaced relative to one another and may be viewed as mesoscopic "grain boundary" sliding. The latter however occurs at least in two phases, the first associated with strain hardening, the second accompanied with strain softening.

Similarly, Travé et al. (2000) reported two microfracture phases in the El Guix anticline (South-Pyrenees). During the first stage, a network of discontinuous microfractures developed, which allowed only local meteoric fluids to circulate (Fig. 5.21a). In the second stage, a continuous thrust fault formed, facilitating now regional fluids to migrate (Fig. 5.21b). With respect to the terminology of this study, the first microfracture stage could correspond to the thrust initiation phase, whereas the second microfracture stage could be linked with the underthrusting phase.

Based on micro-structural work in the Chartreuse district of the French Alps Butler and Bowler (1995) concluded that thrusts evolve through a strain- or displacement-rate cycle (Fig. 5.22). During the first phase thrust 1 is active at high rates whereas, thrust zone 2 deforms at significantly lower rates through an array of minor thrusts (Fig. 5.22a). In the second phase, displacement is transferred to thrust zone 2 (Fig. 5.22b). While thrust 2 has fully developed and deforms at a high rate, thrust 1 has moved into a slow strain rate field (Fig. 5.22c). This evolution is consistent with the conceptual model of an accretion cycle, which predicts low strain rates during the thrust initiation and the re-activation phase (Fig. 5.22a, c) and high strain rates during the underthrusting phase (Fig. 5.22b).

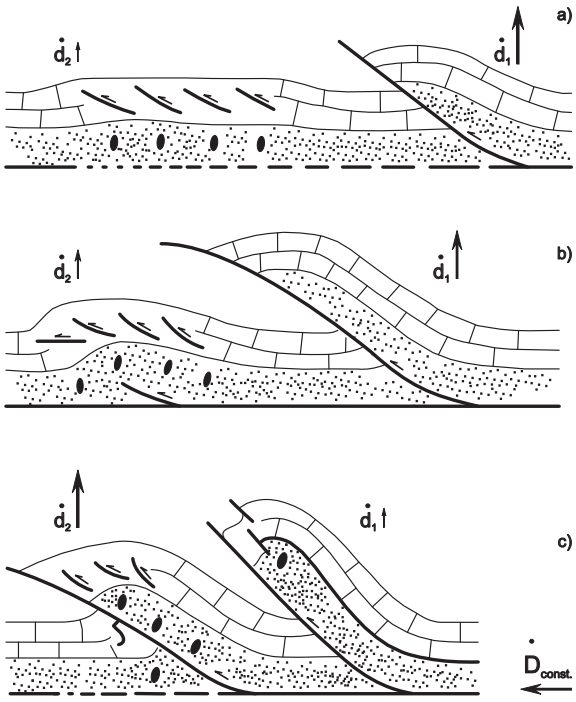

Figure 5.22: Strain (displacement) rate cycle of thrusts. The bulk displacement rate D is assumed to be constant. See text for explanation. Modified after Butler and Bowler (1995).

Meigs et al. (1996) reconstructed the displacement evolution of the South-Pyrenean Sierras Marginales thrust, which is very similar to the

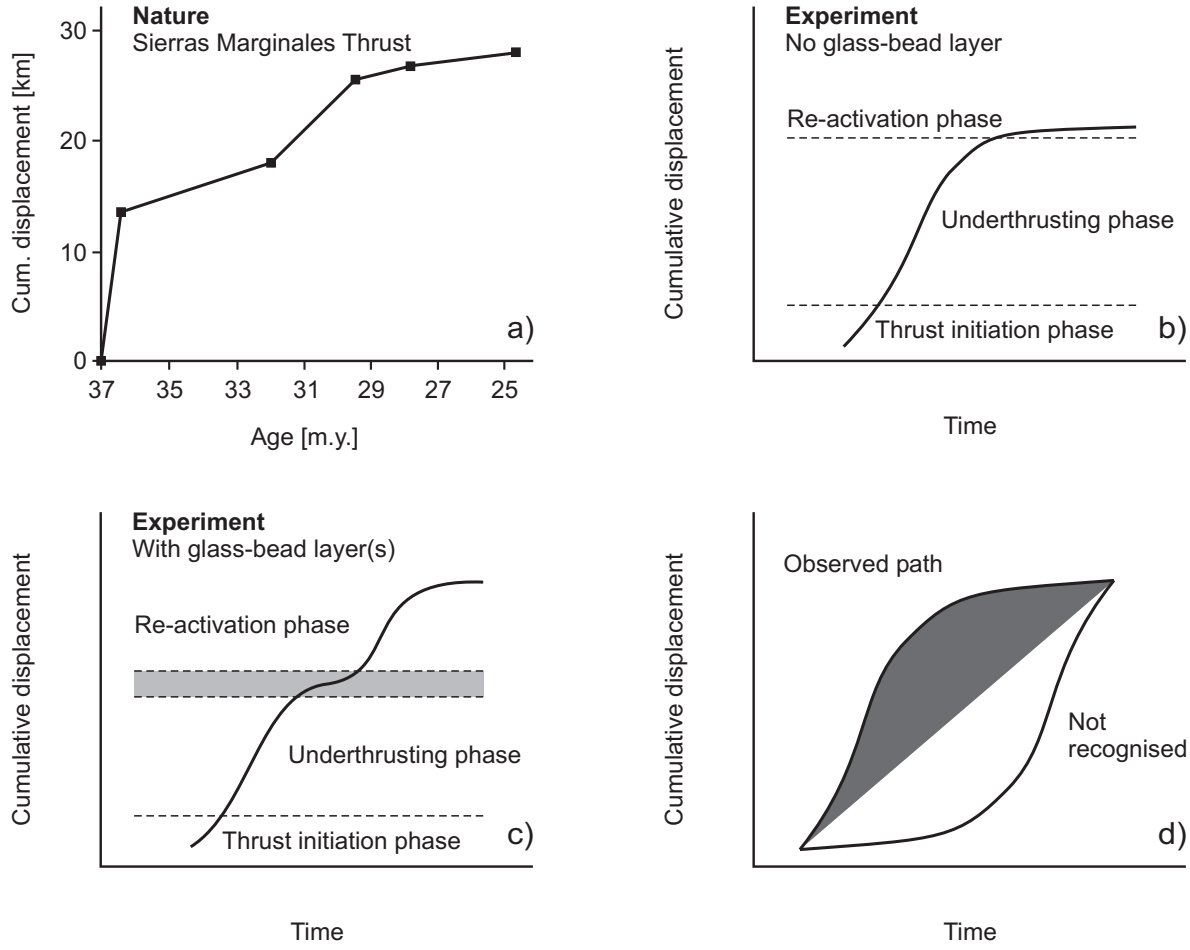

Figure 5.23: (a) Cumulative displacement of the Sierras Marginales Thrust, Southern Pyrenees. Modified after Meigs et al. (1996). Solid squares indicate data points. (b) and (c) show cumulative displacement of thrusts derived from sandbox experiments. Dashed lines in (b) and (c) mark phase boundaries. Gray line in (c) indicates temporal offset between underthrusting and re-activation phase. Note similarity between experimentally derived thrust length evolution and natural pendant. (d) Cumulative deformations paths may indicate that only paths within the dark shaded area are realised by deformation. This in turn might suggest that deformation through time follows a diffusion law, similar to erosion.

displacement histories observed in the bivergent sand-wedges (Fig. 5.23). They further proposed that the displacement transfer from internal to external thrusts is a continuous process, rather than a step-wise sequence of formation, displacement, and de-activation of thrusts. This conclusion is consistent with the one derived from the experiments. Therefore, box-functions of the displacement through time (Jordan et al., 2001) should be invoked with care.

Based on balanced cross-sections Jones et al. (2004) investigated the Eocene to Oligocene Catalan fold and thrust belt. They proposed a thrust sequence, which is concordant with the conceptual model of an accretion cycle (Fig. 5.24).

There are thus several lines of evidence from a variety of methodological approaches as well as from field studies, which provide direct and indirect support for the postulated conceptual model of an accretion cycle. Implications of this model shall be addressed in section (5.4).

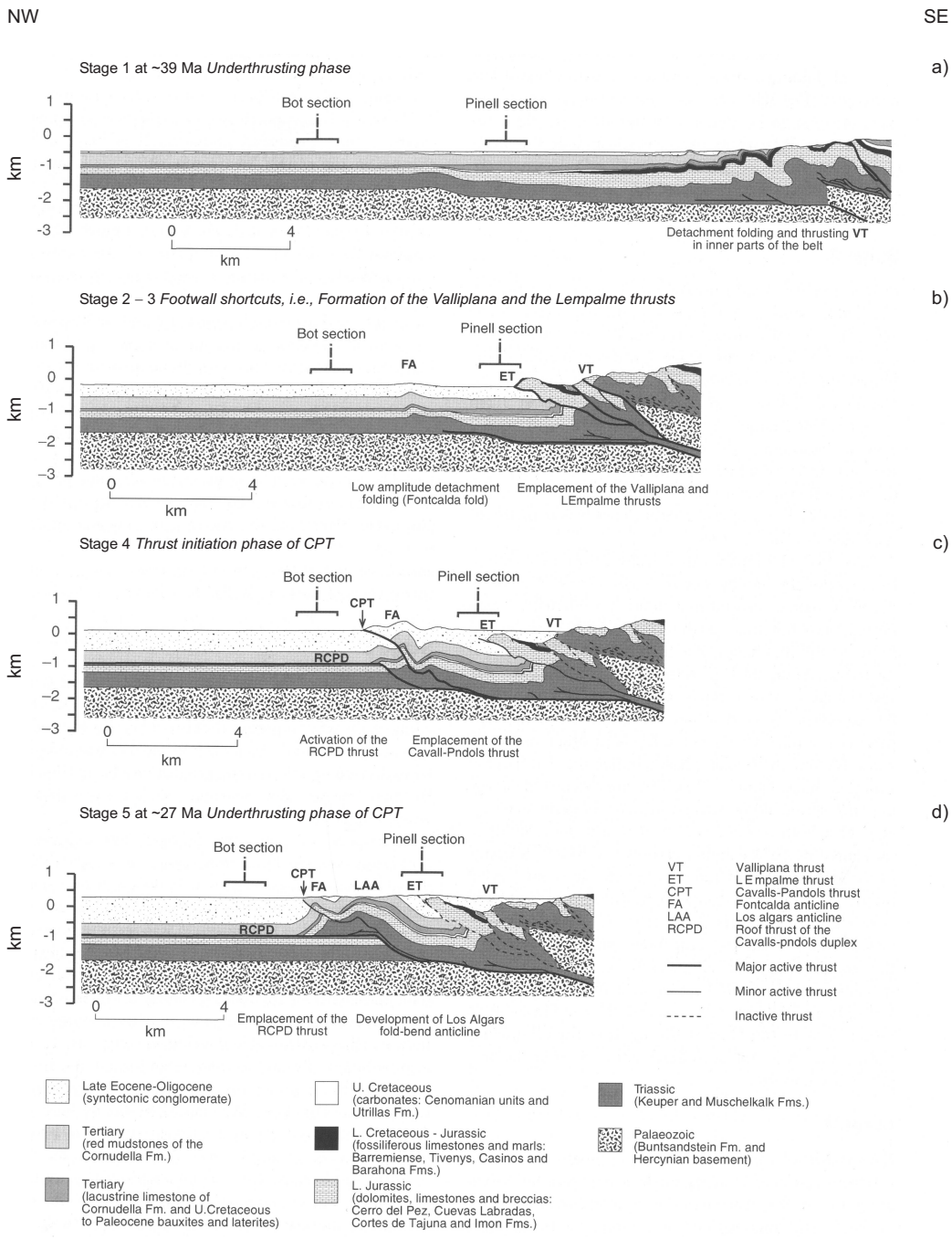

Figure 5.24: Sequential evolution of the central part of the Catalan Coastal Range derived from balanced cross-sections. Time interval is $\sim 10 Ma$. Stages 1 to 5 are based on provenance analysis and other sedimentological data of syntectonic strata, taken at the Bot and at the Pinell section. Own interpretation with respect to the phase within the accretion cycle is given in italics. (a) Probably underthrusting phase. (b) Footwall shortcuts, i. e., the formation of the Valliplana and Lempalme thrusts. Thereby the basal detachment propagates towards the foreland. (c) Thrust initiation phase of the Cavalls-Pandols Thrust, whereby the previous deformation front is still active, i. e., Lempalme thrust. (d) Underthrusting phase of the Cavalls-Pandols Thrust. Note that the hinterland lacks any thrust activity. Modified after Jones et al. (2004).

5.3.3 The timing of thrust initiation

In the previous section the accretion cycle was considered as an internal clock of bivergent-wedge deformation. However, what controls the duration of each accretion cycle and is it predictable? We therefore introduced the sample standard deviation of the wavelength of frontal accretion s_{fw}, which is thought to measure the temporal regularity of the initiation of forethrusts within the pro-layer (Table 5.1). s_{fw} provides thus an estimate of the variability of the time span taken up by individual underthrusting phases. Consequently the term wavelength is used (Fig. 5.3). This method puts more emphasis on the timing of thrust initiation rather than the horizontal distance between two successive ramp segments, commonly referred to as thrust spacing (Marshak and Wilkerson, 1992). A constant timing, i. e., a low s_{fw} value indicates that the wedge response to accretion by internal deformation is similar for every accretion cycle, as outlined in the previous section. High s_{fw} values suggest that this response varies with each accretion cycle. In terms of the minimum work theory this means that internal deformation is favoured until the initiation of a new thrust within the pro-layer would consume less work (section 3.4).

Introduction of one or more weak layers or the simulation of erosion (chapter 6) reduces the internal strength of the pro-wedge and may thus lead to prolonged internal deformation and finally to higher s_{fw} values. This is supported by experimental observations since s_{fw} increases as the number of glass-bead layers increases as well (Table 5.1). Experiment 9.25 deviates only apparently from this trend, since the basal and the internal detachment are both activated twice, which results in a high s_{fw} value. Further support for this interpretation is derived from the OOSD index (Table 5.1). A high OOSD index indicates more internal deformation, i. e., more thrusts are synchronously active (Fig. 5.18). Again, experimental data suggest that the OOSD index increases if the number of glass-bead layers increases as well (Table 5.1).

If one considers flexure and each glass-bead layer as degrees of freedom, then a further interpretation emerges. Experiment 9.15 and 9.25 with one degree of freedom have the lowest, experiment 9.05 and 9.35 with two degrees of freedom have higher and experiment 9.20 with three degrees of freedom attains the highest OOSD index. A similar trend can be recognised for s_{fw}.

It follows from the above discussion that the variability of the duration of each accretion cycle does strongly depend on the boundary conditions, i. e., the numbers of degrees of freedom. Thus, with a given setup, one prescribes the relative magnitude of piggy-back, synchronous, and out-of-sequence thrusting. If the number of degrees of freedom is low, then piggy-back thrusting dominates, while more degrees of freedom promote synchronous and out-of-sequence thrusting. This conceptual model of degrees of freedom might explain the high variability found in natural fold and thrust belts (Butler, 1987; Morley, 1988; Boyer, 1992; Butler, 2004), puts emphasis on boundary conditions in nature and in modelling techniques and finally sheds light onto what is often considered as “local conditions”.

5.3.4 The spacing of thrusts

The spacing of thrusts as defined by Marshak and Wilkerson (1992) is fairly constant throughout the experiments (Fig. 5.12). Its dependence on the depth to the detachment is evidenced in experiment 9.20 and 9.25. This agrees with results from field studies (Soto et al., 2002; Morellato et al., 2003; Marshak, 2004), analytical considerations (Bombolakis, 1986; Mitra and Boyer, 1986; Goff and Wiltschko, 1992; Panian and Wiltschko, 2004) as well as analogue simulations (Liu et al., 1992; Marshak and Wilkerson, 1992; Mulugeta and Koyi, 1992; Boyer, 1995; Koyi, 1995; Corrado et al., 1998; Gutscher et al., 1998; Soto et al., 2002) that thrust spacing depends on the thickness of the incoming layer, its internal and basal properties as well as on the surface slope of the wedge.

Furthermore, figure (5.3) indicates that the aspect ratio of the thrusts, i. e., length (spacing) of a thrust divided by the thickness of the incoming layer is approximately 3, which is very similar to values observed in fold and thrust belts (Onno Oncken pers. com., (2005)). This finding provides additional support for the correct scaling of the mechanics of sand-wedges.

The variability of thrust spacing in the experiments is highest for those, where the basal detachment of the thrusts is located above the conveyor belt and lowest, where this detachment is located within the internal glass-bead layer (Table 5.1). The difference in peak friction between glass-beads and sand is significantly higher (6.2° or 17.6 %) than the difference in peak friction between the sand and the conveyor belt (3.3° or 9.5 %). Thus, the glass-bead layer provides always the weakest zone in the incoming layer and is thus prone to be used as a detachment. Additionally, a glass-bead layer is spatially better defined, if sieved carefully, than the sand – conveyor belt interface. The resulting shear zone is more or less straight in the former and shows an anatomising pattern in the latter case (Jürgen Adam pers. com., (2002)). Such irregularities of a detachment surface have been observed along the Barbados Ridge décollement, which crosscuts other stratigraphic levels, but remains within a 10 m to 20 m wide zone of significantly increased porosity and fluid content (Bangs et al., 1999; DiLeonardo et al., 2002). From a broader perspective, topographic irregularities of the basement surface upon which a wedge is thrusted can focus the nucleation of thrusts and thus influence their respective spacing (Wiltschko and Eastman, 1983; Bombolakis, 1986). On the other hand, Dixon (1982) noted that the regular spacing of thrusts in the Idaho-Wyoming-Utah thrust belt developed over a featureless basement surface. Similarly, Sean Willett (pers. com., (2005)) suggested that thrust spacing is more similar, if basal friction is low.

Interestingly, experiment 9.15 shows a low variability with respect to the temporal regularity of forethrust formation, but shows at the same time a high variability of thrust spacing (Table 5.1). The opposite holds true for experiment 9.20. We therefore hypothesise: (i) that thrust spacing is dominantly controlled by the mechanical properties of the incoming layer and its detachment, which agrees with previous studies (e. g., Marshak and Wilkerson, 1992), and (ii) that the timing of thrust initiation is controlled by wedge internal deformation, which in turn depends on the number and orientation of weak zones, the degree of flexure or erosion (section 6.3.3), i. e., the degrees of freedom as postulated earlier. This would further imply that no direct link between the spatial regularity of the spacing and the temporal regularity of the timing exists. Therefore, neither observation can be used to infer the other and may finally point to end-member behaviour, i. e., time predictable and spacing predictable. A similarity with earthquake models might appear (Fig. 5.25). However, the latter assumes a constant slip rate, whereas the end-member scenarios derived from the experiments does not. Accordingly, both models would describe similar observations, but at different spatial and temporal scales.

5.3.5 Frontal accretion in the retro-wedge

One of the critical issues associated with the strain transfer in bivergent wedges is the occurrence of frontal accretion within the retro-wedge (stage IV). Factors thought to control this phenomenon, include the geometry of the backstop (Davis et al., 1983; Byrne et al., 1988; Lallemand et al., 1994; Wang and Davis, 1996), the strength of the backstop (Byrne et al., 1993), the strength of the backstop base (Pfiffner et al., 2000), and finally a subduction reversal (Del Castello et al., 2004). However, based on experimental results we propose that additional factors have to be taken into account. As demonstrated in section (5.2), we found that strain accumulation along the retro-shear zone

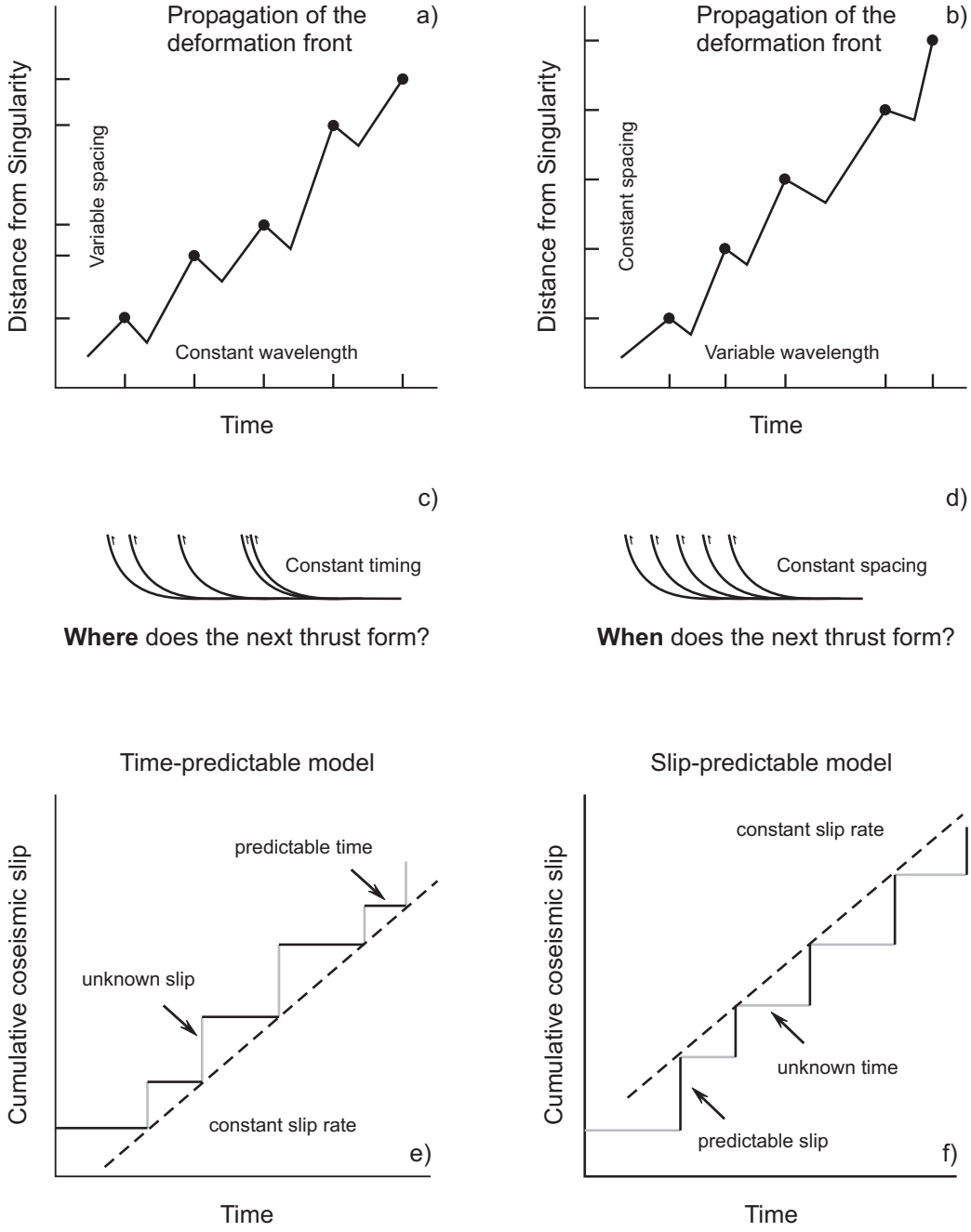

Figure 5.25: Postulated end-member behaviour: (a) Timing of thrust initiation is constant but not its spacing. (b) Thrust spacing is constant but not its timing. (c) and (d) are schematic imbricate fans, which may result from (a) and (b) respectively. It follows that a regular geometry does not necessarily indicate a constant timing, which suggests that one cannot use geometry to unequivocally infer a temporal regularity of thrust initiation. Both end-members bear some similarity to earthquake models: (e) Time-predictable model is based on a constant stress level at which failure occurs. Stress drop and slip magnitude are unpredictable, but given previous slip, time until the next earthquake with unknown slip is predictable. (f) Slip-predictable model is based on a constant stress level at the end of an earthquake. Given time since the last rupture, magnitude of slip is predictable. Both earthquake models assume a constant slip rate, which is not the case or only for very short time increments within the end-member scenarios derived from the experiments. (e) and (f) are redrawn from Burbank and Anderson (2001).

does not only depend on the phase within the accretion cycle, but also on:

i. *Length of the pro-wedge.* The strain history of all monitored retro-shear zones (section 5.2) follows a damped oscillation, which can be correlated with the lateral growth of the pro-wedge (Fig. 5.17). The latter in turn leads to an increasing number of weak zones, i. e., thrusts, between the deformation front and the retro-shear zone. As noted earlier, these thrusts have to be strain-hardened first, before the entire pro-wedge and the axial-zone can slip upon the retro-shear zone. We therefore hypothesise that a growing pro-wedge evokes strain dissipation.

ii. *Strength of the pro-wedge.* Among all experiments, experiment 9.20, with its two glass-bead layers, shows the lowest magnitude of incremental e_{xy} at the retro-shear zone (Fig. 5.16, Fig. 5.17). Additionally, experiment 9.20 has the highest OOSD as well as the highest s_{fw} index (Table 5.1) among all experiments and shows a rather distributed pattern of finite e_{xy} (Fig. 5.15). These observations in conjunction with the strength profile (Fig. 4.8) are therefore thought to indicate that the respective pro-wedge has a significantly lowered integrated strength.

iii. *Mechanical properties of the detachment of frontal accretion within the pro-wedge.* Figure (5.17d) reveals that the mechanical properties of the basal detachment of the flat-topped box-anticlines within the pro-wedge exert an influence on the respective response of the retro-shear zone. Thus, the latter "knows" the mechanical properties of the former.

It follows that a force balance approach sensu Gutscher et al. (1998), to calculate the width and the height of the axial-zone/retro-wedge necessary to initiate frontal accretion within the retro-wedge, would have to invoke (i) those thrust, i. e., at least four, which are active during an accretion cycle, (ii) a measure of the length of the pro-wedge, (iii) a measure of the integrated strength of the pro-wedge, and (iv) if erosion is simulated (chapter 6), a measure of the topography/load through time. This is at present not possible and it is left for future studies to explore solutions.

It is finally pointed out, that the surface slope of all retro-wedges remained rather uniform throughout the entire wedge evolution and was always at or close to the angle of repose. A lower-tapered retro-wedge sensu Willett et al. (1993) could not be observed since frontal accretion within the retro-wedge started late during experiments.

5.3.6 Parameter combinations

The observation of frontal accretion within the retro-wedge has been made for three out of five experiments considered at this stage. In the previous section, we proposed that a decrease of the integrated strength of the pro-wedge has at least retarded if not inhibited this process to occur. A similar effect is observed, if β is zero. To start with, this observation agrees well with published results from experiments with similar kinematic boundary conditions, e. g., Storti et al. (2000) and McClay and Whitehouse (2004). Although, experiment 9.25 has only $120\,cm$ of convergence, a similar experiment by U. Schönrock (experiment 11.7, GFZ Laboratory 2004) with $150\,cm$ of convergence revealed the same result – no frontal accretion within the retro-wedge. Given that the only difference between experiment 9.25 and 9.05 is flexure, we conclude that flexure might promote frontal accretion within the retro-wedge. Experimental evolution reveals that flexure leads to a rotation of the already steep retro shear-zone towards the pro-wedge. At the same time, the glass-bead layer, located at the base of the upper plate, rotates as well, attaining a more inclined orientation. It follows from Mohr-circle considerations,

Parameter	Promoting upper plate failure	Retarding upper plate failure
Flexure [9.15; 9.25]	✓	
Integrated strength of upper plate [*]	If low	If high
Upper plate thickness [4.06†]	If thick	If thin
Basal detachment [9.04§]	If weak	If strong
Integrated strength of lower plate [9.20]	If similar to upper plate or higher	If low
Amount of material addition via convergence [4.03‡]	If high	If low
Retro-wedge erosion [9.06]	✓	
Pro-wedge erosion [9.09]		✓

* Numerical simulations by Beaumont et al. (2000) show that increased retro-crust strength reduces retro-thrusting.
† Upper plate is two times thicker than the lower plate.
§ Experiment 9.04 is similar to experiment 9.05 but lacks the basal glass bead-layer and also frontal accretion within the retro-wedge. Results from Wang and Davis (1996) indicate a coincidence between a flat lying backstop covered with a plastic sheet (μ_b = 0.43) and frontal accretion within the retro-wedge. In contrast, a flat lying backstop covered with sandpaper ($\mu_b > 0.65$) prohibited frontal accretion within the retro-wedge.
‡ Experiment by Jürgen Adam (1999). Setup mediates between 9.05 and 9.25. Frontal accretion within the retro-wedge emerged after 210 cm of convergence.

Table 5.3: Parameters, which either promote or retard frontal accretion within the retro-wedge.

that a higher differential stress is required to keep the steeper retro-shear zone active, whereas it is the opposite for the glass-bead layer. Within this respect, Boyer (1995) found that a higher β, which results from increased flexure, requires less internal shortening to attain a critical taper, and a larger percentage of tectonic shortening translates into frontal advance of a thrust belt. It is highlighted that the role of flexure in controlling the kinematics of bivergent orogens has not been addressed (Teresa Jordan pers. com., (2004)).

The above considerations as well as the ones from section (5.3.5) indicate that the initiation of the frontal accretion within the retro-wedge cannot be assigned to a unique parameter combination. For example, the absence of flexure retards frontal accretion within the retro-wedge, whereas prolonged convergence promotes it (Table 5.3). Similarly, increased flexure in combination with a higher basal friction of the upper plate base evokes frontal accretion within the retro-wedge, above the glass bead-layer (Experiment 9.02, Fig. 5.26), which is consistent with the observations of Wang and Davis (1996).

These results do further indicate that some parameters tend to promote, others tend to retard frontal accretion in the retro-wedge (Table 5.3). Whether frontal accretion within the retro-wedge occurs, depends finally on the combination of the above mentioned and other parameters such as fluid flow, cementation processes, sedimentation or a polarity reversal of the convergence geometry. Thus, the observation "frontal accretion within the retro-wedge" can be imagined as a cloud in multi-dimensional parameter-space, where several combinations of parameters lead to the same result. This might indicate that a hierarchical order of parameters does not exist.

The only condition for frontal accretion within the retro-wedge to occur is that the strength of the initiation of a thrust within the upper plate is lower than the re-activation of the retro shear-zone, provided that a sufficient stress transfer into the upper plate takes place. How to achieve this condition is a question of parameter combination.

5.3.7 Self-similar growth

The CCW concept predicts that only critically tapered wedges grow in width and height proportional to the convergence (t) by $t^{0.5}$ (Dahlen, 1990). However, none of the bivergent sand-wedges showed such a self-similar growth. Only the lateral growth of two pro-wedges (Experiments 9.15, 9.20) was proportional to the conver-

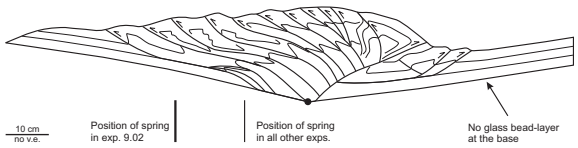

Figure 5.26: Experiment 9.02 has the same mechanic stratigraphy as experiment 9.05, but has a 50 % higher deflection of the lower plate. The latter results from a longer distance between the free end of the lower plate and the spring (44 *cm*), compared to 30 *cm* in all other experiments. Note, that the internal glass-bead layer within the upper plate acts as a detachment, which was not observed in the other experiments.

gence (t) by $t^{0.5}$ (Table 5.1). This would indicate that all studied bivergent sand-wedges grew not self-similar but self-affine, which agrees with observations from Koyi (1995).

Given that a self-similar growth results from the critical state only, we suggest that the bivergent sand-wedges within this study are not critical. Interestingly, a self-similar growth of sand-wedges has, to our knowledge never been reported from any sandbox simulations, nor from natural orogens. Further support for the postulation that the bivergent sand-wedges are not critical, is derived from critical taper considerations. Given that a basal shear-zone is active throughout the experiment, its mechanical properties are thought to be best described by the stable-dynamic friction. Additionally, we follow Lohrmann et al. (2003) and suggest that the internal mechanic properties of the pro-wedge are as well best described by stable-dynamic friction.

Based on these assumptions we find that the pro-wedge of experiment 9.15 is in the stable field throughout its evolution (Fig. 5.27), which agrees very well with the above observations. Other assumptions with respect to the material properties would lead to the postulation that the pro-wedge is over-critical and should fail by extension, which was not observed. These calculations were only made for experiment 9.15, since the knowledge about the internal material properties of a pro-wedge, which contains one or two glass-bead layers, is not adequate. The above observations however, could also indicate that the CCW concept, which assumes an ideal Mohr-Coulomb material is not sufficiently appropriate to describe the mechanics of a sand-wedge, which clearly shows strain hardening and strain softening processes.

5.4 Implications and predictions for natural bivergent wedges

In this study we have investigated the influence of the imposed kinematic boundary conditions such as different mechanic stratigraphies or the degree of flexure on the kinematic evolution of bivergent sand-wedges. Given the scale invariance of brittle behaviour, we propose that the obtained results are applicable to (i) bivergent orogens, e. g., the European Alps, the Pyrenees; to (ii) fold and thrust belts, e. g., the Western Altiplano Thrust Belt (Elger et al., 2005) and to (iii) accretionary prisms, e. g., the Sunda Arc (Silver and Reed, 1988), and the Mediterranean Ridge (Le Pichon et al., 2002). Accordingly, the implications derived from the experiments bear no specific spatial scale and may be tested upon their validity in all three settings. However, some caution must be taken while transferring and applying our results to bivergent orogens, since we focus only on lower temperature orogens, where brittle behaviour prevails. High exhumation rates may finally lead to the removal of the highest strength part of the continental crust, which significantly reduces its integral strength. At this stage ductile processes might start to dominate (Zeitler et al., 2001; Koons et al., 2002).

Four staged evolution of bivergent wedges. Based on the assumption that one continental plate descends beneath the other during orthogonal continent-continent collision, we suggest a four-staged evolutionary model for the growth of bivergent orogens. An initial symmetric, crustal scaled pop-up (stage I) or backfold is followed by the formation of a proto pro-wedge, where frontal ac-

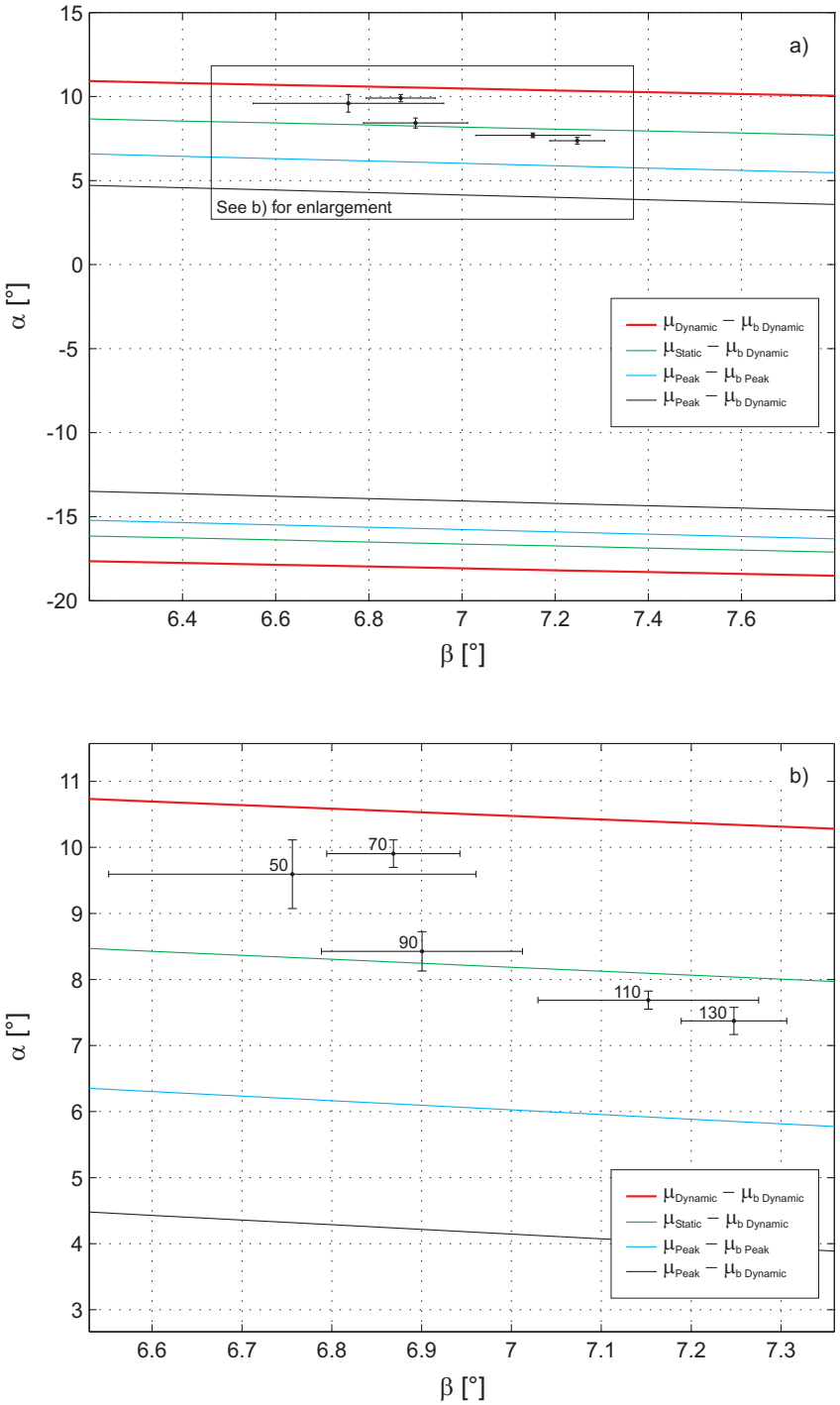

Figure 5.27: (a) Theoretical stability fields, using equation (3.10), for four combinations of frictional properties of the wedge interior and its base. Data are taken from ring-shear measurements. μ denotes the coefficient of internal and μ_b denotes the coefficient of basal friction respectively. (b) Enlargement of (a). Numbers associated with data points are *cm* of convergence (Experiment 9.15). If one assumes that μ and μ_b are best described by the dynamic stable friction, than the entire pro-wedge of experiment 9.15 is within the stable field throughout its evolution.

cretion dominates (stage II). Further convergence leads to an increase of the kinematic and topographic asymmetry. Basal accretion commences, if a mid-crustal detachment is present (stage III). During stage IV, frontal accretion within the retro-wedge occurs, which may drive the orogen back to more symmetric conditions. This model can be tested against balanced orogen-scale cross-sections and we suggest that the transition from stage II to stage III, i. e., onset of basal accretion as well as the transition from stage III to stage IV, i. e., onset of frontal accretion within the retro-wedge, should be identifiable. The latter is explained in terms of the strength contrast between the upper plate and the retro-shear zone. Thus, neither a reversal of the convergence geometry nor specific backstop geometries are necessary for frontal accretion within the retro-wedge to occur.

Self-similar growth. A self-similar growth was neither observed in this study, nor has been reported from any sandbox experiment. This agrees with Lohrmann et al. (2003), who proposed that only the frontal part of a sand-wedge is in a critical state. Additionally, based on balanced cross-sections from the South Pyrenean fold and thrust belt, Meigs and Burbank (1997) showed that the spatio-temporal distribution of deformation, as well as the magnitude of α and β through time are decoupled and not simply related. Thus, the assumption that an entire orogen is in a critical mechanic state should be made with great care if at all. We therefore propose that orogen-scaled mass-budget calculations, which focus on erosion and assume a self-similar growth, should be limited to the most frontal part of an orogenic wedge.

Accretion cycle. The proposed conceptual model of an accretion cycle integrates previously unrelated observations such as the periodicity of thrusting, the associated topographic evolution, and the cumulative slip evolution of thrusts. In addition this model predicts:

The occurrence of a thrust initiation, an underthrusting and a re-activation phase. Thereby, the latter phase is coeval with the thrust initiation phase of the following accretion cycle. Depending on the kinematic boundary conditions, the re-activation phase maybe temporally offset from the underthrusting phase.

We found that the magnitude of strain accumulated at any given structure within a bivergent wedge systematically varies with the accretion cycle. The accretion cycle is therefore considered as an internal clock of wedge-scaled deformation and resulting surface uplift. Such a mechanism could explain the irregular earthquake cycle along the Aksu thrust, Tien-Shan (Hubert-Ferrari et al., 2005) and the irregular initiation and re-activation of thrusts within the southern Pyrenees (Meigs, 1997). It follows that geodetic, paleoseismologic, and geologic estimates of fault slip must not necessarily be the same, as found, e. g., in the Tien-Shan (Coutand et al., 2002). Thus, interpolation of slip rates from different temporal scales and resultant predictions of recurrence intervals of earthquakes can only be successful, if the phase within the accretion cycle is known. Accordingly, the ability to differentiate between individual events (earthquakes) or phases within an accretion cycle will guide our perception on how deformation is distributed in space and time. We therefore suggest that an accretion cycle should be sampled with $\frac{1}{4}$ of its duration, to resolve its three-partite evolution (Fig. 5.28). Also, each structure might have its own b-value (seismicity), which changes through time, as accretion proceeds. Since a thrust is not necessarily in the same phase within the accretion cycle along its strike, differences in seismicity may result. We therefore propose that such along strike changes should be taken into account, if seismic hazard potential is evaluated. It follows that changes of kinematic boundary conditions or of the climate/erosion scheme do not need to be invoked to explain the spatio-temporal variability of strain accumulation.

Observed strain histories of thrusts do not resemble box-functions. The former however, would overestimate strain accumulation during the thrust initiation and during the re-activation phase, but underestimate strain accumulation during the underthrusting phase. Thus, the temporal dependence of strain-partitioning on the phase within the accretion cycle should be taken into account, while restoring deformed sections and simulating hydrocarbon maturity in fold and thrust belts, which commonly assume that only one structure is active for a certain time (Rouré et al., 2004).

Based on the cumulative strain histories of thrusts either within sand-wedges or within fold and thrust belts (sections 5.1, 5.2), we further hypothesise that strain accumulation follows a diffusion law (Fig. 5.23). Such a behaviour would be very similar to the one predicted for erosion (Burbank and Beck, 1991).

Spatial and temporal offset of cause and response. We observed a temporal offset between the initiation of a new thrust within the pro-layer (cause) and the resulting "strain-pulse" at the retro-shear zone (response). This could be one explanation for the temporal offset of $\sim 5\,Ma$ between the emplacement of the Helvetic nappes above the Aar massif and enhanced rates of back-thrusting along the Insubric Line (Schlunegger and Willett, 1999). However, the magnitude of strain transfer between the pro- and the retro-wedge decreases while the former grows laterally. Thus, during later stages of orogenic evolution this strain transfer might not be detectable.

Fluid flow. Depending on their permeability and porosity evolution, thrust faults may either provide important fluid conduits or act as barriers (Travé et al., 2000; Badertscher et al., 2002). While the former can promote the formation of precious ore deposits, such as the mesothermal gold mineralisations in the Southern Alps of New Zealand (Craw et al., 2002; Upton et al., 2003; Craw and Campbell, 2004), the latter can lead to compartmentalisation of a fold and thrust belt,

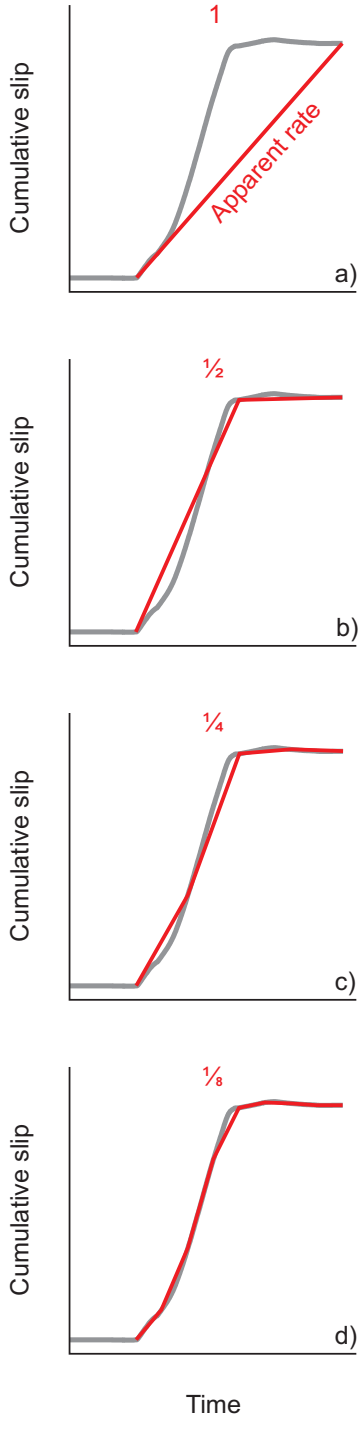

Figure 5.28: Sampling interval controls estimates of cumulative slip. Original data in grey; (a) Resulting rate, if only pre- and post-tectonic strata are dated; (b-d) Increasing resolution approaches "real data", given that age constrains are equally distributed in time.

which may aid the accumulation of hydrocarbons (Moretti et al., 2000). In addition, and probably most importantly, we documented that the phase within the accretion cycle determines the degree of connectivity between thrusts and their maximum incremental e_{xy}. We therefore speculate that the source and the availability of fluids may vary with the accretion cycle as well. Observations from the El Guix anticline in the Southern Pyrenean foreland basin (Travé et al., 2000) would support such a prediction (section 5.3.2). Within this context, it is interesting to note that Muir-Wood (1994) linked the secondary migration of hydrocarbons with seismic pumping (Sibson, 1994). Thus, the former may be enhanced during phases of accelerated seismicity, i. e., the underthrusting phase. It follows that the accretion cycle concept may help to constrain hydrocarbon exploration strategies.

Topographic evolution. The distribution of surface uplift within orogens should indicate at least two domains, one that comprises the pro-wedge and one that includes the axial-zone and the retro-wedge. Topography in the former is highly segmented and reflects individual accretion cycles. On the contrary, continuous vertical stacking and retro-ward translation of basally accreted duplexes results in a smooth and dome-like shape of the second topographic domain. Thus, care should be taken, while interpreting surface uplift rates from different parts of an orogen. We additionally highlight that basal accretion episodes have not led to a detectable trace within the ISU and we speculate that this might be similar in nature. However, basal accretion leads to the bending of the upper surface, resulting in extension. The respective faults and syntectonic sediments might finally provide indirect inside to the timing and magnitude of basal accretion. Thereby, other processes, e. g., late orogenic collapse have to be ruled out.

Each accretion cycle is associated with a surface uplift wave, which decreases in magnitude with increasing distance from the deformation front. Nevertheless, the increase in ISU observed in the second topographic domain, may reach up to 400 % and takes place between a thrust initiation phase and the late stages of the respective underthrusting phase. Such an increase in ISU should be therefore detectable in natural systems.

A surface uplift wave would also successively rejuvenate the relief of more internal parts of an orogen. We therefore propose that a detailed provenance analysis might detect the successive unroofing and erosion of a certain suite of hinterland lithologies and may thus trace a surface uplift wave. Results from a field study within the Catalan Coastal Range (Jones et al., 2004) indicate that the detection of such a surface uplift wave is possible. In addition, a certain lag time between relief rejuvenation and the appearance of the respective clasts within the foreland is expected and has been also proposed by Tucker and Slingerland (1996). These authors invoked this mechanism to explain the apparent delay between uplift of the Tibetan Plateau ($\sim 14 + Ma$) and the onset of rapid sedimentation in the northern Indian Ocean ($\sim 12 Ma$).

ISU above a ramp segment of a forethrust does not increase linearly with time and a thrust reactivation can lead to a tenfold increase of the respective ISU. Therefore, changes of the kinematic boundary conditions or of the climate/erosion scheme do not need to be invoked to explain such variability. A similar non-linear growth has been reported from a late Quaternary anticline in New Zealand (Jackson et al., 2002) and from numerical simulations (Bernal et al., 2004). Additionally, Masaferro et al. (2002) concluded that the Neogene-Quaternary growth of the Santaren anticline (Cuban fold and thrust belt) was characterized by several tectonic uplift pulses of different duration and intensity, interrupted by periods of variable duration in which no fold growth occurred. We therefore suggest that a self-similar growth assumption for thrust induced topography should be treated with care.

Heisenberg's principle of uncertainty? Experiments show that the mechanical properties of the detachment control the variability of the spacing of thrusts, whereas the number of degrees of freedom such as flexure, weak zones and erosion determine the relative magnitude of internal deformation versus propagation of deformation and thus the timing of thrust initiation and its variability. We therefore envisage an end-member scenario, where the spacing is constant but not the timing and vice versa. In the former, one would know the location of thrust initiation but not its timing, in the latter one would know the timing of thrust initiation but not its location. It follows, that a spatial regularity is not necessarily associated with a temporal regularity. One should be therefore very careful, while deriving one information from the other. A similar model has been put forward for earthquakes, i. e., time-predictable versus slip-predictable. Although these processes are entirely deterministic as opposed to quantum mechanics, the uncertainty associated with the prediction of the timing and location of the next slip event results from the incomplete knowledge of the mechanic state of each grain or fault.

We found that an observation like frontal accretion within the retro-wedge can be explained with several parameter-combinations and a parameter-hierarchy may not exist. This raises the challenge to decide whether two observations are coincidentally or if a causal relation exists between them.

5.5 Implications for erosion experiments

The results derived from the first experimental series are now used to constrain the kinematic boundary conditions of the second experimental series, which is aimed at investigating the influence of the location of erosion with respect to the convergence geometry and the mode of erosion (distributed or focused) on the kinematics of bivergent sand-wedges. Two arguments can be raised in favour of incorporating flexure. First, as shown in chapter (3), flexure is besides deformation and surface processes one of the major controlling processes of mountain building. Second, natural orogens show a distinct ratio of 2 to 3 between the length of the pro- and the length of the retro-wedge (Silver and Reed, 1988; Vietor and Oncken, 2005). Sandbox models of bivergent wedges without flexure reveal ratios that are lower than two (Malavieille (1984) and our own experiment 9.25). Those experiments with flexure show ratios between 2.5 and 3 (Table 5.1) and are thus similar to the ones observed in nature. The contemporaneous occurrence of frontal and basal accretion is a common observation in natural bivergent wedges, e. g., Pyrenees, European Alps (Beaumont et al., 2000; Pfiffner et al., 2000). Thus, experiment 9.05 is used as a reference for all "erosion" experiments (chapter 6).